Spray Characteristics of Free Air-on-Water Impinging Jets

Y. Xia, M. Alshehhi, Y. Hardalupas(*)， L. Khezzar

Mechanical Engineering Department, Khalifa University of Science and Technology, Petroleum Institute, Abu Dhabi, United Arab Emirates
(*) Mechanical Engineering Department, Imperial College London, London, U.K.
Corresponding email address: lkhezzar@pi.ac.ae

ABSTRACT

Characteristics of a water-on-air free impinging jets atomizer is investigated in this study by means of flow visualization using high speed photography with Phase Doppler Anemometry (PDA) to measure the droplet size and velocity. Spray structures and breakup process are illustrated with the aid of images captured for the water and air jets impinging at 45°. The breakup length of the water jet decreases with the increase of the air to liquid jet momentum flux ratio (*ALMFR*) and remains constant for values of *ALMFR* larger than 1. Divergence and deflection spray angles increase rapidly with the air to liquid momentum ratio (*ALMR*) and then remain constant for values of *ALMR* larger than 4. A larger impinging angle leads to a smaller breakup length and larger spray angles. PDA results indicate that the planar distribution of droplet size is symmetrical around the Y-axis, but not around the X-axis. Smaller droplets are located near the spray center, but their location varies for different experimental conditions, with the minimum value of D_{32} = 50 μm and increasing to around 120 μm at the outer region of the spray for conditions Q_L = 100 mL/min, $\dot{m}_g$ = 13.5 g/min and θ = 45°. The spatially-averaged Sauter mean diameter (SMD), representing the average size of droplets over a cross section plane of a spray, is defined and it remains the same at any cross section of the spray operating with the same experimental conditions. Spatially-averaged SMD is found to decrease with the increase of *ALMR*. Droplet mean velocity is the largest at the position downstream of the air jet exit (14 m/s at a plane of z = 75 mm in the spray with Q_L = 100 mL/min, $\dot{m}_g$ = 13.5 g/min and θ = 45°) and decreases gradually with increasing distance from the point where droplets with the maximum velocity are located. The study makes up for the spray visualization of the study of a single water jet impinging on a single air jet externally, and provides more information on the spray characteristics of this injector, which will contribute to the evaluation of improved computational models and improved injector design.

Key words: Impinging jets; Atomization; Flow visualization; PDA; Droplet size and velocity; Sauter mean diameter

1. Introduction

Liquid jet atomization is encountered in various applications, such as gas turbines, rocket engines and industrial furnaces. In such systems, it is recognized that higher volumetric heat release rates, easier ignition, a wider burning range and less exhaust pollutant emissions can be achieved by reducing the generated mean drop size in most combustion cases (Lefebvre 1985; Rink and Lefebvre 1986). Therefore, understanding of factors affecting the mean drop size and its control is crucial for the design and proper operation of such systems.

The need for improved combustion control has motivated the development of different atomizer configurations to acquire better atomization with high rates of mixing and surface area of liquid fuels, among which twin-fluid atomizers have attracted particular attention since they can lead to satisfactory atomization with relative slow moving liquid (Lefebvre 1988). Numerous studies on various designs of twin-fluid atomizers have been conducted in an effort to derive better understanding of the atomizers' performance and resulting spray characteristics, such as effervescent atomizer (Sovani, et al. 2001, Jedelsky, et al. 2009, Gomez, et al. 2011), air-blast atomizer (Chigier and Farago 1992; Engelbert, et al 1995; Lasheras and Hopfinger 2000; Strasser and Battaglia 2017), air-assist atomizer (Avulapati and Venkata 2013; Inoue, et al. 2013; Avulapati and Ravikrishna 2015; Xia, et al. 2017), flow blurring atomizer (Gañán-Calvo 2005; Simmons and Agrawal 2010, Jiang, et al. 2014; Niguse and Agrawal 2016;), liquid jet in cross flow (Lubarsky, et al. 2012, Kourmatzis and Masri 2015, Jadidi, et al. 2016).

Impinging jets atomizers with one gas and two-liquid jets have also been considered by Avulapati and Venkata (2013) Avulapati and Ravikrishna (2015), and Xia, et al. (2017). In Xia, et al. (2017), the spray characteristics have been quantified. In contrast to this configuration, performance characteristics of another variant of impinging jets atomizers consisting of one liquid jet impinging onto another gas jet have not received equal attention as the other atomizers. So far, according to the authors' knowledge, this configuration of atomizer has only been mentioned by Boden, et al. (1999) and Prabhakaran and Basavanahalli (2013). Boden, et al. (1999) carried out an experimental study of such an air-water impinging jets atomizer using phase Doppler anemometry (PDA) to investigate the effects of air to liquid momentum ratio, impinging angle and initial jet diameter on the atomization efficiency. Increase of liquid flow rate is found to worsen the atomization, while the impinging angle of the two jets did not affect

the atomization efficiency. However, the spray structure is not presented due to the absence of visualization of the liquid breakup process. Prabhakaran and Basavanahalli (2013) recently re-examined characteristics of the spray from such a configuration of gas-liquid impinging injector trying to figure out a unifying parameter that can combine several influencing factors based on results obtained from photography and Malvern particle analyzer. Their results, which contained droplet size information only, indicate that the impinging angle of the jets affects the Sauter mean diameter (D_{32}) of the spray droplets in contrast to previous findings.

In order to shed more light on this configuration of liquid-gas impinging atomizer, a vertical air jet impinging on an inclined liquid jet is considered. The study consists of flow visualization using high speed camera and simultaneous droplet size and velocity measurements with phase Doppler anemometry (PDA). In addition, liquid jet breakup length and spray angles are quantified based on spray images captured by the high speed camera.

The resulting spray from this water-air impinging atomizer is not axisymmetric, and in order to evaluate the atomization efficiency at different conditions independently of the rate of spread of the droplets, which varies with droplet size, it is not enough to solely consider the centerline values of D_{32}, since the droplet sizes away from the centerline can be also varying and are not taken into account when evaluating atomization efficiency. Therefore, a weighted spatially averaged Sauter mean diameter (SMD), integrated over a cross section plane of the spray, is used to quantify the atomization efficiency. This is defined as:

$$\overline{D_{32}} = \frac{\int D_{32}(x,y)G(x,y)dxdy}{\int G(x,y)dxdy} \qquad (1)$$

where $D_{32}(x,y)$ is the local value of the measured SMD at the point (x,y) of the spray, G(x,y) is the local volume flux of the droplets, measured by the PDA, and *dxdy* is the elemental area of the local measurement point inside the spray. The rest of this manuscript contains a description of the experimental setup and measurement techniques, followed by the presentation of the results and conclusions.

2. Experimental set up and measurement techniques

The experiment was conducted at an ambient room temperature of 20 ºC and atmospheric pressure. High speed photography and PDA are separately used to conduct spray visualization and simultaneous droplet size and velocity measurements, respectively.

The schematic of the test rig is shown in Fig. 1, of which the main components include a water-air impinging jets atomizer, the high speed camera and PDA systems.

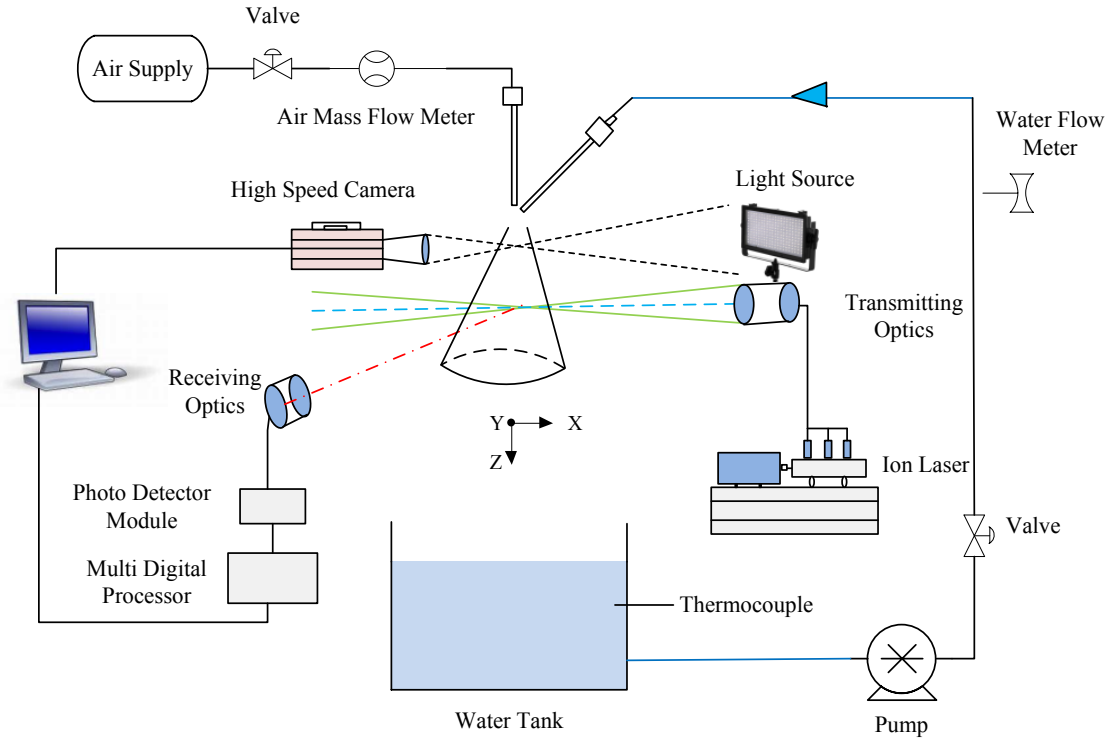

Fig. 1. Schematic of the experimental setup

The air jet is vertical and impinges on an inclined water jet. Water and air flowrates were supplied and controlled independently. A magnetically coupled centrifugal pump, together with a needle valve and a calibrated Omega water flow meter of 1 % accuracy, is employed to transport the water from a tank to the water jet nozzle. Compressed air from the centralized compressor system is supplied to the air jet nozzle and the air flow rate is metered using an Alicat mass flow meter with an accuracy of ±0.3% reading +0.2% F.S. The spray is collected by the water tank after ejection.

The water-air impinging jets atomizer, as shown in Fig. 2, is made of two stainless steel pipes, of which the water pipe diameter is 0.686 mm, while the air pipe diameter is 1 mm. The water and

air pipes are 152.4 and 304.8 mm in length, so the length to diameter ratios *L/d* for water and air jets are 222.2 and 304.8 respectively, ensuring fully developed conditions at the exit of both air and liquid nozzles. The two pipes are fixed onto a manufactured well aligned frame and the distance between the nozzle exit and the geometrical impingement point *O* is 10 mm for both air and water pipes. The impinging angle between the air and water jets is varied by using frames of fixed angles, including 30°, 45° and 60°. A three-dimensional computer-controlled traverse system from TSI with a positional accuracy of 0.01 mm is employed to move the atomizer at different locations. The geometrical impingement point *O* is set as the reference point (0, 0, 0) in a XYZ coordinate system shown in Fig. 2.

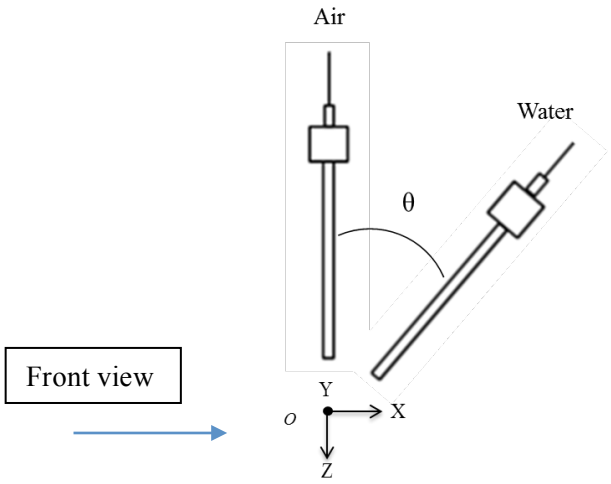

Fig. 2. Configuration of atomizer

Water temperature is monitored by a K-type thermocouple throughout the experiment to ensure that temperature remains constant to avoid any effect of temperature variation.

The high speed camera system consists of a FASTCAM SA3 high speed camera and an LED matrix to provide back illumination. Images were recorded from both the front and side views (namely X and Y directions of Fig. 2) with the software of Photron Fastcam Viewer Ver.352 at frame rates of 15,000 fps and 20,000 fps for far and near-field, respectively, corresponding to resolution of 256×256 and 512×128 pixels leading to spatial resolution of 0.15 mm/pixel and 0.03 mm/pixel, respectively. The spray structure and the way that the water and air jets interact with each other were observed from instantaneous photographic temporal sequences. The water jet breakup length and spray angles have been measured using 50 frames with a public domain, Java-based image processing program ImageJ developed at the National Institutes of Health (Collins 2007; Schneider, et al. 2012) with uncertainties less than 5% of the average values. The

spray angle was measured from binary images converted from the RGB images from the high speed camera by visually identifying the edges of the region occupied by the water droplets. The PDA is a two scattering laser beams and three detectors standard system from TSI consisting of an Argon-Ion laser, transmitting optics, receiving optics, photo detector module (PDM) and multi digital processor (MDP). Detailed information about the PDA system and probe volume characteristics is given in Table 1. The droplet sampling was completed when the number of sampled droplets reached 15,000, based on which the average droplet size and velocity information is quantified. The droplet velocity is obtained from the frequency of the fluctuation of the scattered light intensity of the Laser Doppler Anemometer, based on the proportional relationship between the light intensity frequency, fringe spacing and velocity. The droplet size is obtained from the phase shift that is present between the Doppler signals, which are detected at different locations in space and converted from optical to electrical signals captured by the photo-detectors positioned at selected angles (Husted, et al. 2009).

Table 1. Settings and parameters of the two velocity components PDA system

Transmitting Optics		
Channel	Channel 1	Channel 2
Wavelength (nm)	514.5	488
Focal Length (mm)	500	500
Beam Separation (mm)	20	20
Laser Beam Diameter (mm)	1.7	1.7
Beam Expander (ratio)	2	2
Expanded Beam Separation (mm)	40	40
Expanded Beam Diameter (mm)	3.4	3.4
Fringe Spacing (μm)	6.4364	6.1049
Beam Waist (μm)	96.34	91.37
Bragg Cell Frequency (MHz)	40	40
Phase Doppler Receiving Optics		
RVC Front Lens $f_{.l.}$ (mm)	500	
RVC Back Lens $f_{.l.}$ (mm)	370	
Slit Aperture (μm)	150	
Off-axis Angle (▫)	30	
Droplet Properties		
Scattering Mechanism	Refraction	
Polarization Angle	Perpendicular	
Refractive Index of liquid	1.33	
Droplet Size range (μm)	0.61 - 251.26	

In this study, an L-shape frame is utilized to support and fix the transmitting and receiving optics to achieve good and easy alignment. The systematic accuracy of the droplet size measurement is less than $1\%D_{max}+1\%D_{measurement,}$ and repeatability is 0.5%, while of the droplet velocity is less than 0.2% and repeatability is 0.05% (Lai, et al. 2013). The statistical uncertainties for droplet size and velocity averaged values are about 2% and 1% respectively based on statistics from 15,000 samples. The overall uncertainty of the droplet Sauter mean diameter is estimated to be $\pm$4% and for droplet velocity $\pm$1%.

The experiment was conducted under the operating conditions shown in Table 2. Spray visualization was carried out to study the effects of water flow rates and air mass flow rates. Quantitative PDA measurements were conducted across a spray cross plane to obtain the spatially-averaged SMD (Eq. (1)) and average droplet size and velocity planar distributions.

Several corresponding parameters are defined to present the results better, including air-to-liquid momentum flux ratio (*ALMFR*), air-to-liquid momentum ratio (*ALMR*), Weber number and Reynolds number.

$$ALMFR = \rho_g U_{imp}^2 / \rho_l U_l^2 \tag{2}$$

$$ALMR = \dot{m}_g U_{imp} / \dot{m}_l U_l \tag{3}$$

$$We = \rho_g U_{imp}^2 d_l / \sigma \tag{4}$$

$$Re_l = U_l d_l / \nu_l \tag{5}$$

where ρ_g is the gas density, ρ_l is the liquid density, U_{imp} is gas jet velocity at the impingement point, U_l is liquid jet velocity, $\dot{m}_g$ is the gas mass flow rate, $\dot{m}_l$ is the liquid mass flow rate, d_l is the liquid jet diameter, σ is the surface tension between interface liquid and gas, and ν_l is the kinematic viscosity of liquid. The specific use of the gas velocity at impingement as used by Inoue et al. (2013), would remove influence of the pre-impingement length L to make the present results based on one single value of L = 10 mm independent of it and thus more general.

Table 2. Experimental conditions

Water flow rate (single jet)	50	100	150	200	240

Q_L (mL/min)					
Re_l	1541	3081	4622	6162	7395
Air mass flow rate $\dot{m}_g$(g/min)	4.4	6.7	13.5	27.0	
We	24.	56	227	909	
Jet impinging angle θ (°)	30	45	60		
$ALMFR$	0-6				
$ALMR$	0-17				

3. Results and discussions

This section will present results on spray structure, liquid jet breakup length and spray angle derived from the spray visualization experiments. PDA measurements of mean droplet size, liquid volume flux and mean droplet velocity and the corresponding RMS of velocity fluctuations are considered next.

3.1 Spray structure

Figure 4 illustrates images of the spray at various water and air mass flow rates captured from both front view (F.V. - X-axis of Fig. 2) and side view (S.V. - Y-axis of Fig. 2). The situation at hand is that of an air jet impinging on a liquid jet, where transfer of energy between the two leads to the liquid jet change in topology and break-up.

In order to describe the spray structure clearly, two spray angles are defined in this study, which are the deflection angle β referring to the angle between the water jet axis and the spray centerline, as shown in Fig. 3 (a) and divergence angle α, defined as the angle of the spray in the plane of the Y-along deflection angle center line (face to the spray, not Y-Z), as shown in Fig. 3 (b).. The divergence angle is obtained by measuring the angle from the direction perpendicuar to the Y-Z plane and then converted to the spray plane by multiplying it by cos(β-θ).

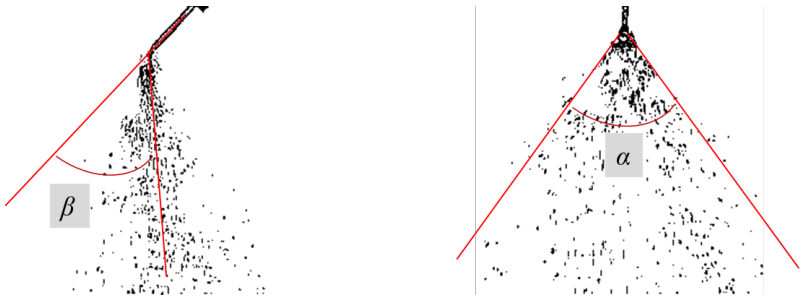

(a) (b)

Fig. 3. Spray angles (a) deflection angle β; (b) divergence angle α

For a fixed water flow rate, the beneficial effect of an increase in air mass flow rate in promoting atomization is clearly evident in the figures presented in Fig. 4. With the increase of mass flow rates, the water jet becomes a flapping sheet, breaks up into ligaments and subsequently into much smaller droplets. The spray divergence angle, as illustrated in the images captured from the front view, increases with the air mass flow rates, as also does the deflection angle. The air jet with a larger Weber number leads to better atomization.

Several flow regimes can be identified from the example instantaneous images of Fig. 4. At water flow rates larger than 200 mL/min and air mass flow rates less than 4.4 g/min, the water jet keeps traveling almost unperturbed along its original direction and behaves in a manner similar to the wind-induced regime of a single jet (Leroux, et al. 1996). At $\dot{m}_g$ = 4.4 g/min, a flapping water sheet can be observed in the near field of the spray at water flow rates of 100 and 150 mL/min. The water jet then bends off its original direction to some degree. With the increase of air mass flow rates, some ligaments are generated from the flapping sheet, as for the case of $\dot{m}_g$ = 6.7 g/min and Q_L = 100, 150 and 200 mL/min. Upon further increase of the air mass flow rate, the ligaments break up forming fragments that stabilize into drops under the aerodynamic influence of the atomizing and ambient gases. At $\dot{m}_g$ = 13.5 and 27.0 g/min for some water flow rates, the water jet is penetrated immediately at the impingement point. Both the spray divergence and deflection angles increase with the air mass flow rates at a fixed water flow rate, but effects of water flow rates are not considerable at air mass flow rates larger than 13.5 g/min.

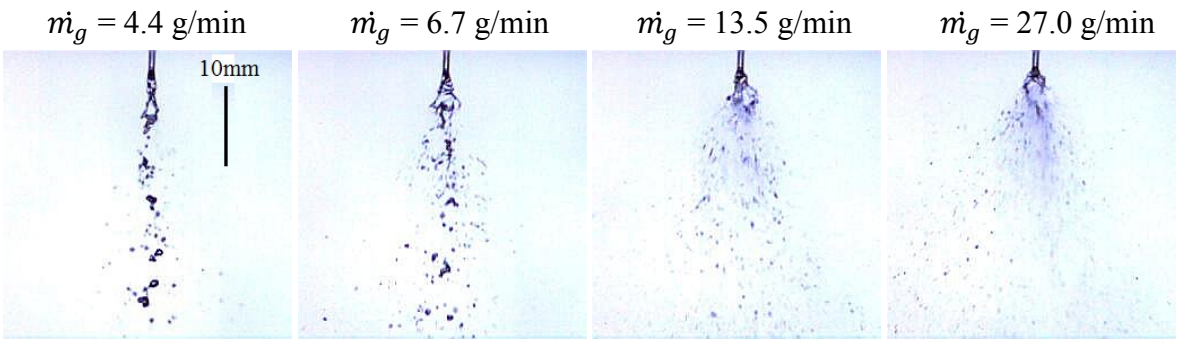

F.V.

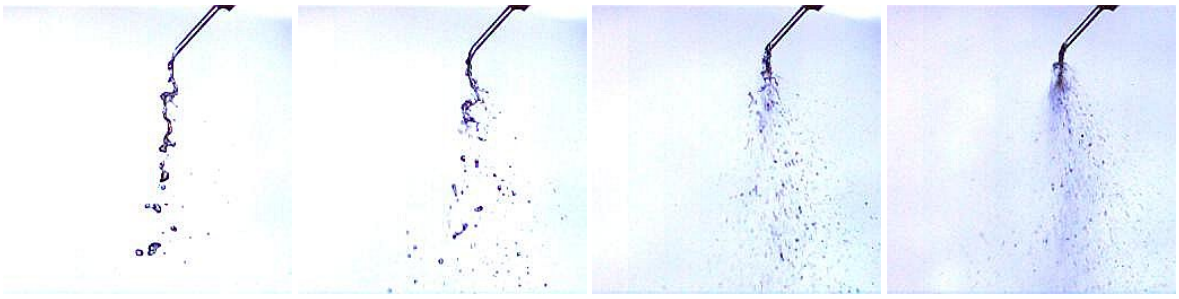

S.V.

Q_L= 50 mL/min; Re_f= 1541

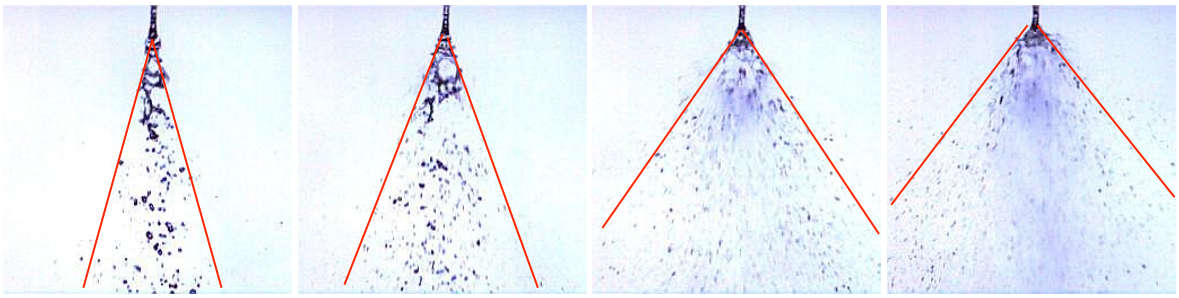

F.V.

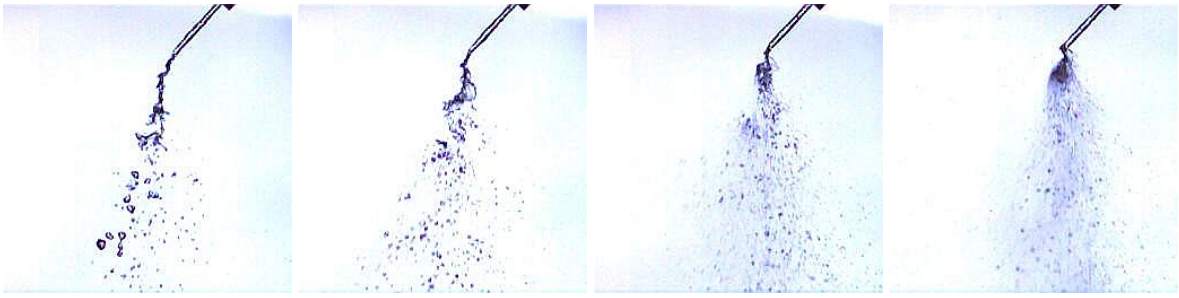

S.V.

Q_L= 100 mL/min; Re_f= 3081

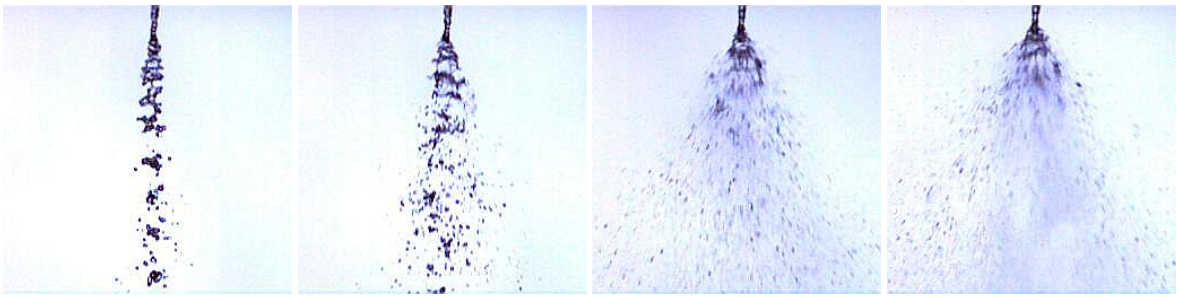

F.V.

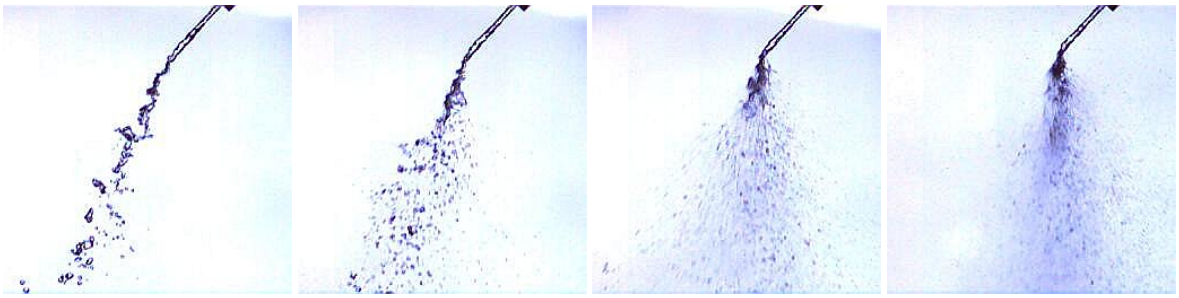

S.V.

Q_L= 150 mL/min; Re_f= 4622

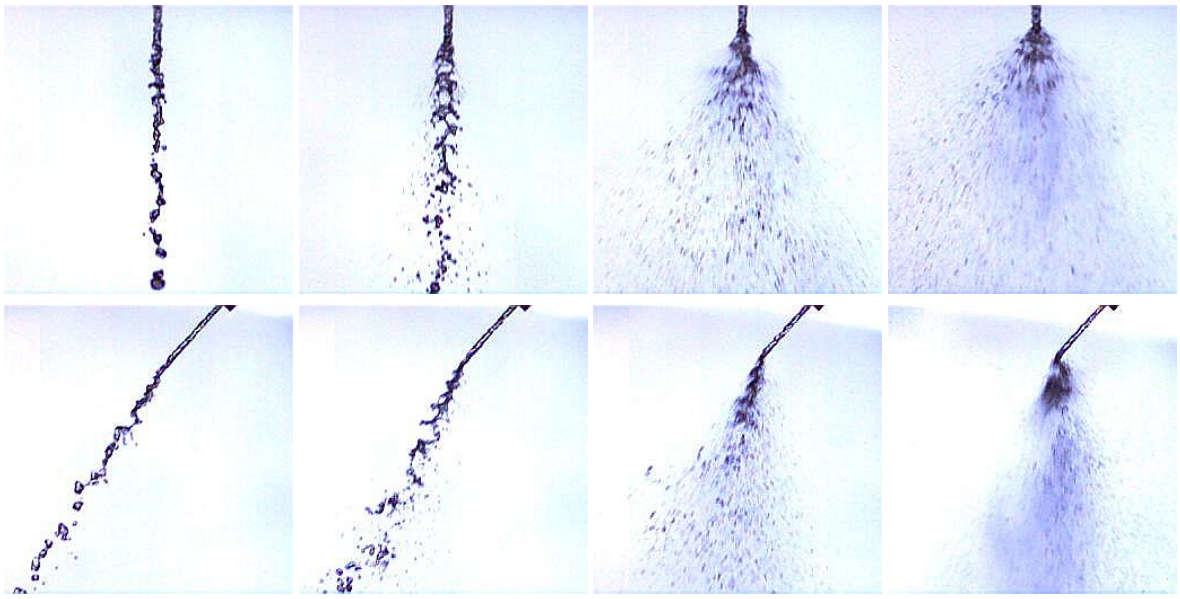

Q_L= 200 mL/min; Re_l= 6162

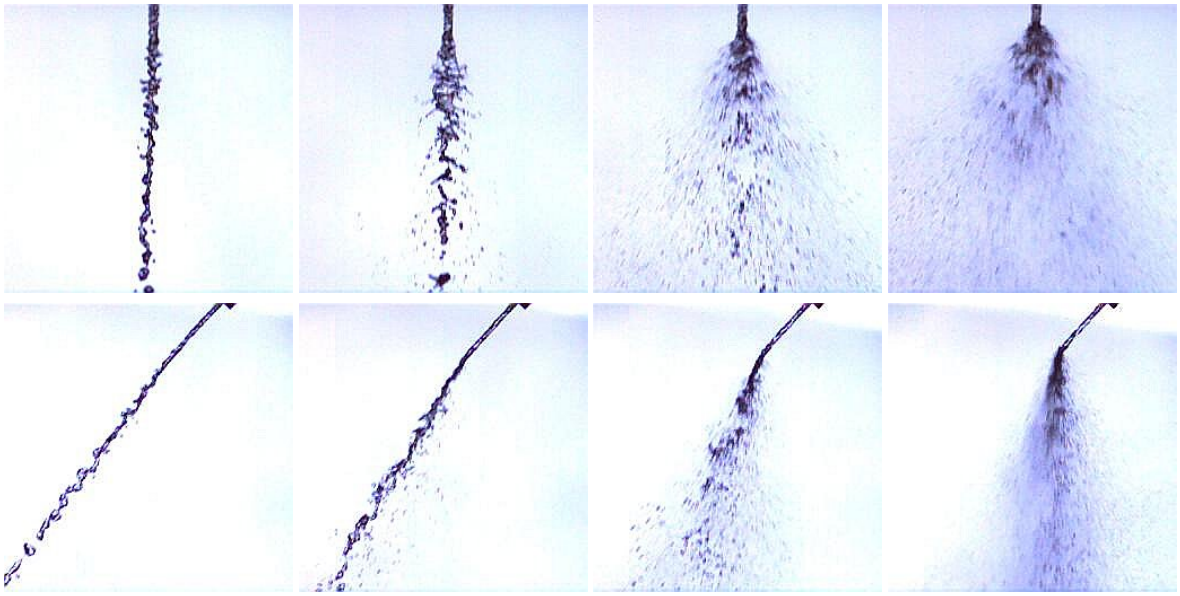

Q_L= 240 mL/min; Re_l= 7395

Fig. 4. Images of the spray structure for jets impinging angle θ = 45° (F.V. refers to front view X-axis of Fig. 2, S.V. refers to side view – Y-axis of Fig. 2)

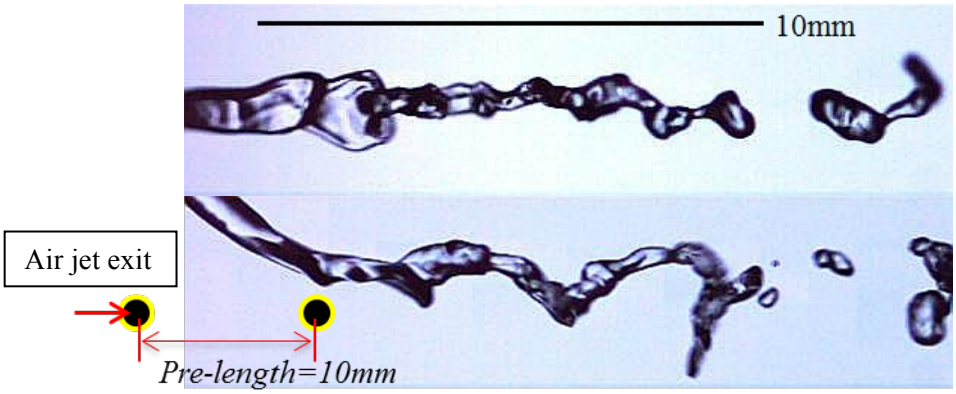

$\dot{m}_g$ = 4.4 g/min; *We*= 24; ALMFR= 0.50

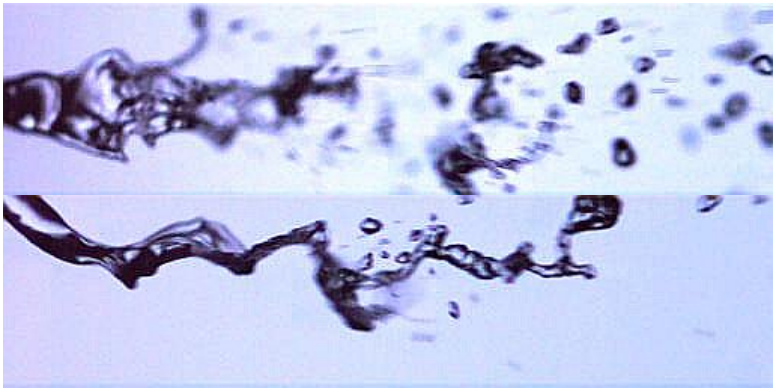

$\dot{m}_g$ = 6.7 g/min; *We*= 56; ALMFR= 1.17

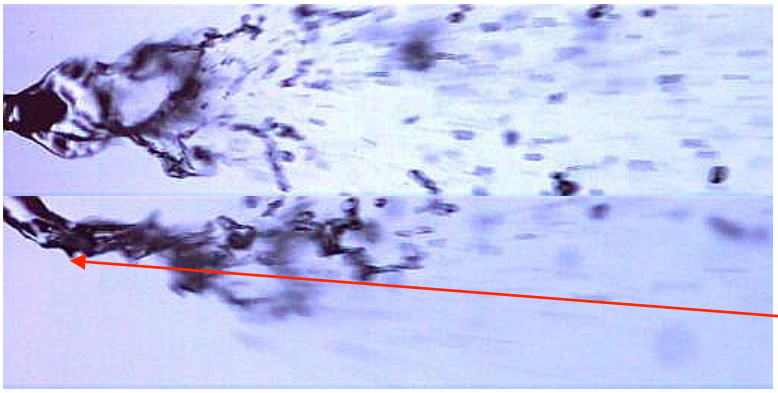

$\dot{m}_g$ = 13.5 g/min; *We*= 227; ALMFR= 4.75

$\dot{m}_g$ = 27.0 g/min; *We*= 909; ALMFR= 19.01

(a) Q_L = 50 mL/min; Re_l= 1541

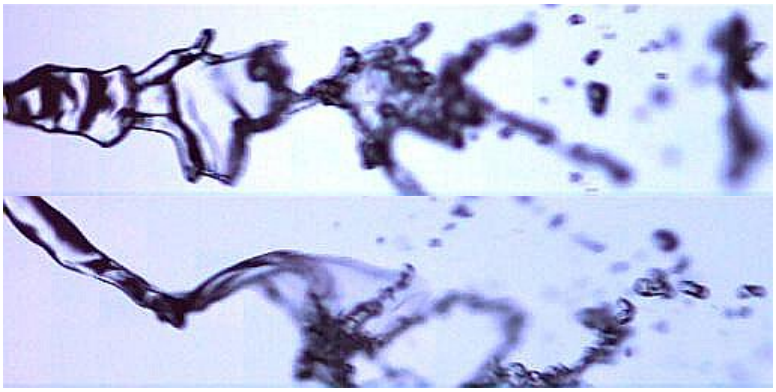

$\dot{m}_g$ = 4.4 g/min; *We*= 24; ALMFR= 0.13

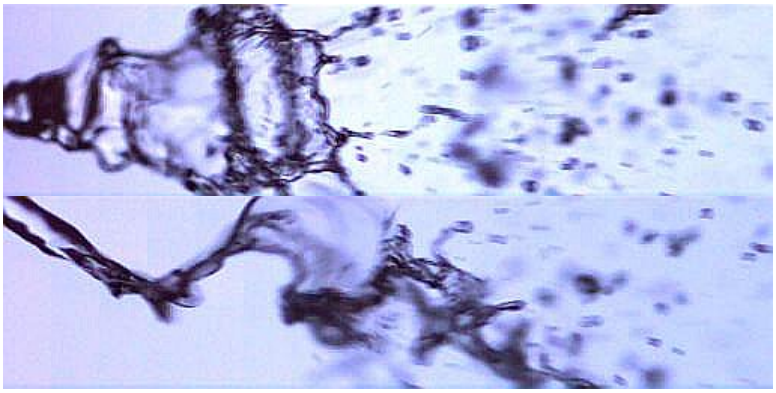

$\dot{m}_g$ = 6.7 g/min; *We*= 56; ALMFR= 0.29

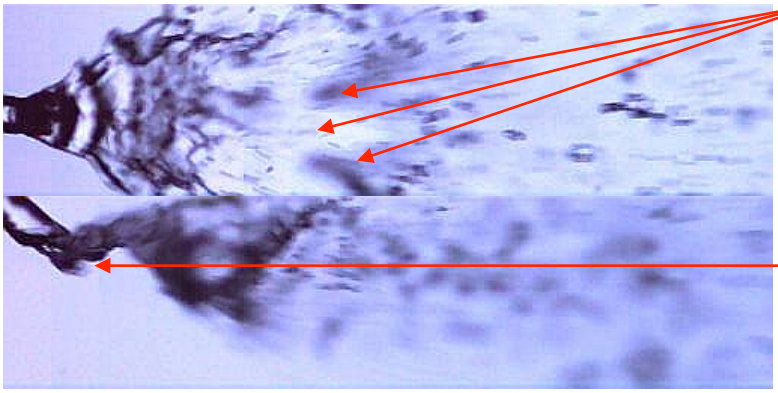

$\dot{m}_g$ = 13.5 g/min; *We*= 227; ALMFR= 1.19

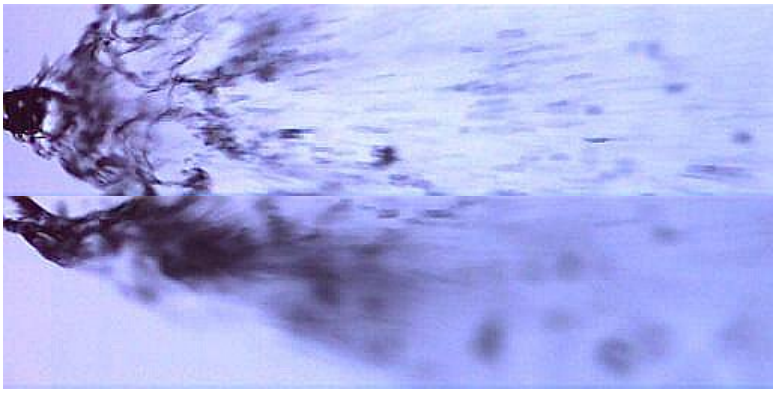

$\dot{m}_g$ = 27.0 g/min; *We*= 909; ALMFR= 4.75

(b) Q_L = 100 mL/min; Re_l= 3081

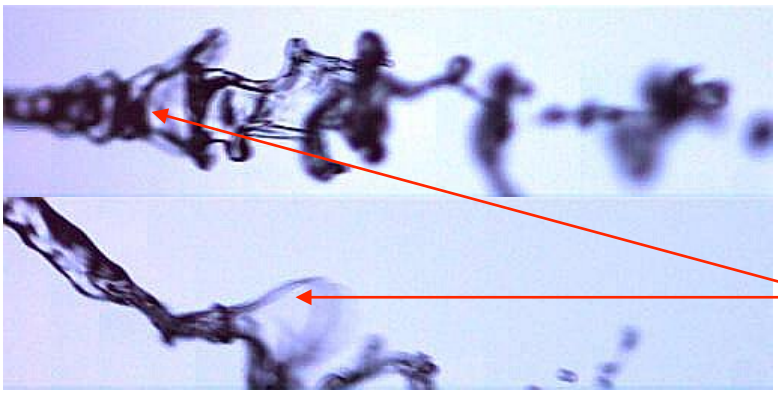

$\dot{m}_g$ = 4.4 g/min; *We*= 24; ALMFR= 0.06

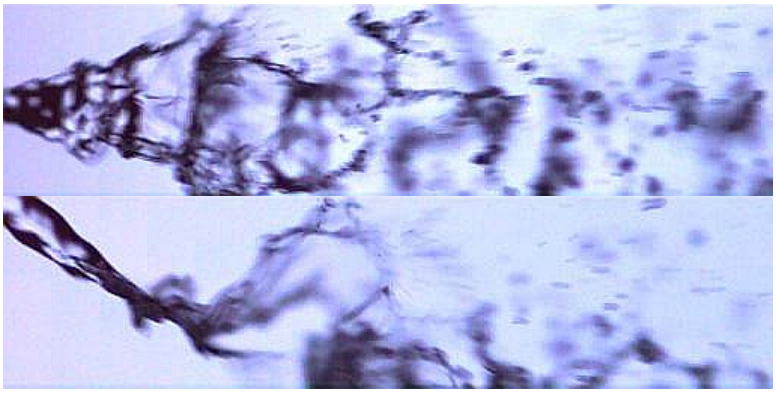

$\dot{m}_g$ = 6.7 g/min; *We*= 56; ALMFR= 0.13

$\dot{m}_g$ = 13.5 g/min; *We*= 227; ALMFR= 0.53

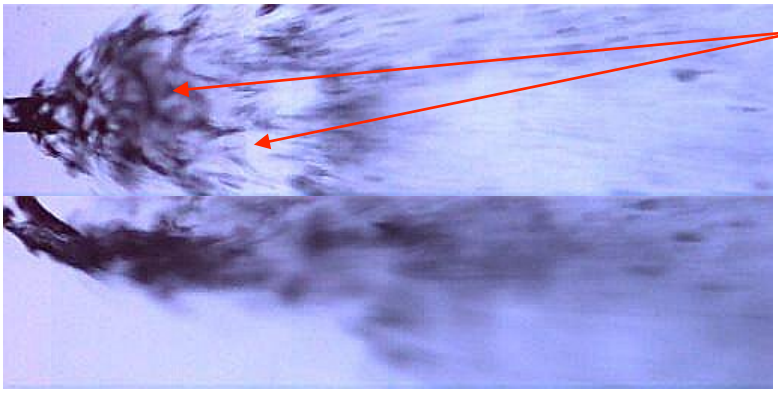

$\dot{m}_g$ 27.0 g/min; *We*= 909; ALMFR= 2.11

(c) Q_L = 150 mL/min; Re_l= 7395

Fig. 5. Magnified images of the liquid jet for jets impinging angle θ= 45°, (a) Q_L = 50 mL/min; (b) Q_L = 100 mL/min; (c) Q_L= 150 mL/min

Magnified images of the near field of the liquid jet flow, as shown in Fig. 5, reveal some details of the breakup process. We describe below the different mechanisms taking place in the near field region, where the two jets meet and interact. On Fig. 5 liquid and gas flow rates, as well as *We* number and *ALMFR* are also reported. At low gas and liquid flow rates, Q_L = 50 mL/min, and $\dot{m}_g$ = 4.4 g/min, the liquid jet deforms in a spiraling form with breakup of large blobs of liquid. The creation of liquid sheets is almost non-existent. At a gas flow rate of $\dot{m}_g$ = 6.7 g/min, it can be observed that the creation of liquid sheets is surrounded by thick rims and ligaments. Under the action of aerodynamic pressure, the liquid sheets are blown to form bags or membranes. These bags and membranes later break up into a range of liquid drop sizes. At higher flow rates, the interface where the air jet impinges on the liquid jet becomes wavy leading to Rayleigh breakup. Just downstream, liquid fibers leading to the generation of small droplets can be observed. It is also interesting to note the existence of patches of concentrated liquid, see

Fig. 5 (b). As noted by Lasheras and Hopfinger (2000), the existence of such patches is related to the motion of large scale structures of the gas jet shear layer, which are responsible for the detachment of liquid sheets and ligaments. These later are then advected downstream and interact with the turbulent air motions. The flow behavior in this case exhibits a characteristic unsteadiness in liquid void fractions referred to as "the super-pulsating mode", see Chigier and Farago (1992). It is also interesting to note that at relatively large values of *ALMFR* typically greater than about 1, atomization is finer. This can also be noticed from Fig. 4 and brings into play the *ALMFR* threshold value of 1, which assumes a particular significance as discussed below in sec. 3.2 following the reasoning of Inoue et al (2013).

Figure 6 illustrates the temporal evolution of the liquid jet break up for Q_L = 50 mL/min and $\dot{m}_g$ = 4.4 g/min. One can observe for this particular case the creation of the liquid sheet and subsequent generation of liquid membrane and its break up.

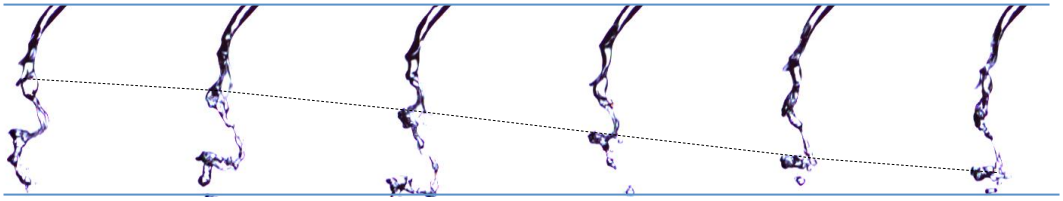

Fig. 6. Time series visualization of the liquid jet development (time interval is 5.337×10^{-4} s)

Hopfinger (1998) generated a break-up regime map for co-axial air blast atomizers using the *Re-We* space which removes reference to the particular liquids used. This map is shown in Fig. 7 with the identified regimes in the present study using water. Bearing in mind that boundaries in flow regime maps are not always precisely identified, the membrane and fiber break up regimes appear to correspond well to those for a liquid jet in a coaxial flow.

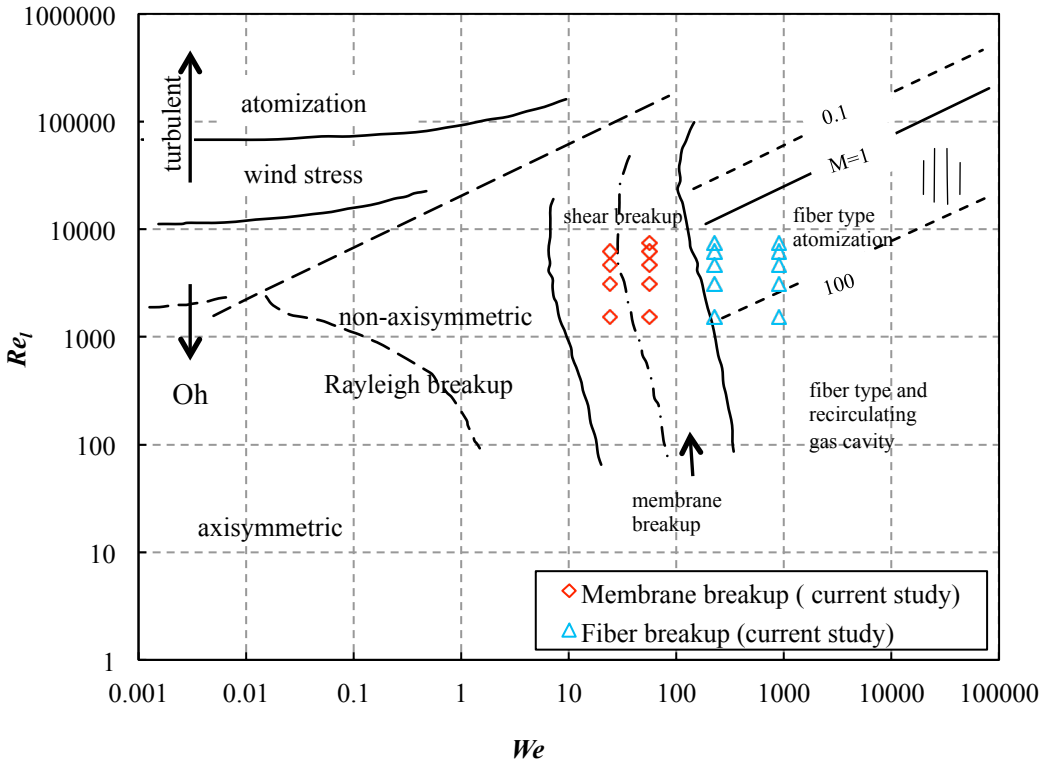

Fig. 7. Breakup regimes in the parameter space Re_l – *We* (Hopfinger 1998)

3.2 Liquid breakup length

The breakup length of the liquid jet is important for the development of computational models that attempt to predict the spray behavior and for industrial applications, due to the fact that the aerodynamic drag for liquid jet and droplets are different. The breakup length, as shown in Fig. 8, is defined as the distance from the geometric impingement point to the position where the water column becomes discontinuous. Fig. 9 presents the breakup length for cases of jets impinging angles of 30°, 45° and 60° as a function of *ALMFR*, as defined in Eq. (2), in order to compare current results with correlations from the literature for coaxial atomizers by Leroux, et al. (2007) and Lasheras and Hopfinger (2000).

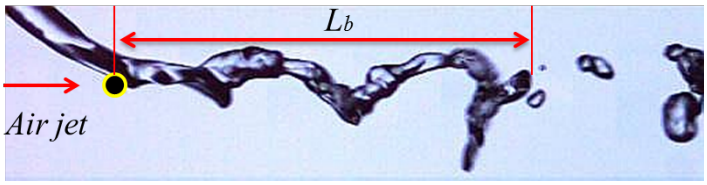

Fig. 8. Breakup length of the jet

For values of *ALMFR* lower than about 1, the breakup length L_b/D_L decreases sharply from a maximum value of about 20 and then tends to level towards a constant value for *ALMFR* larger than 1. The effect of the impingement angle appears to be negligible at very low values of *ALMFR* and the results for angles of 45º and 60º are very close to each other beyond a value of *ALMFR* of 1. The general trend of the present measurements is similar to the previous correlation results.

Inoue et al (2013) considered a similar configuration and argued that at the stagnation (impingement) point the gas jet is able to penetrate the liquid jet if the total pressure of the former is larger than that of the latter. Their reasoning leads them to derive an equivalent threshold value for *ALMFR* >=1, which when satisfied leads to enhanced atomization with finer droplets. In Fig. 9 it can be seen that for *ALMFR* greater than 1 the break up length remains constant since the gas jet penetration has already taken place at the value of 1 and there is no further change in the liquid jet global topology.

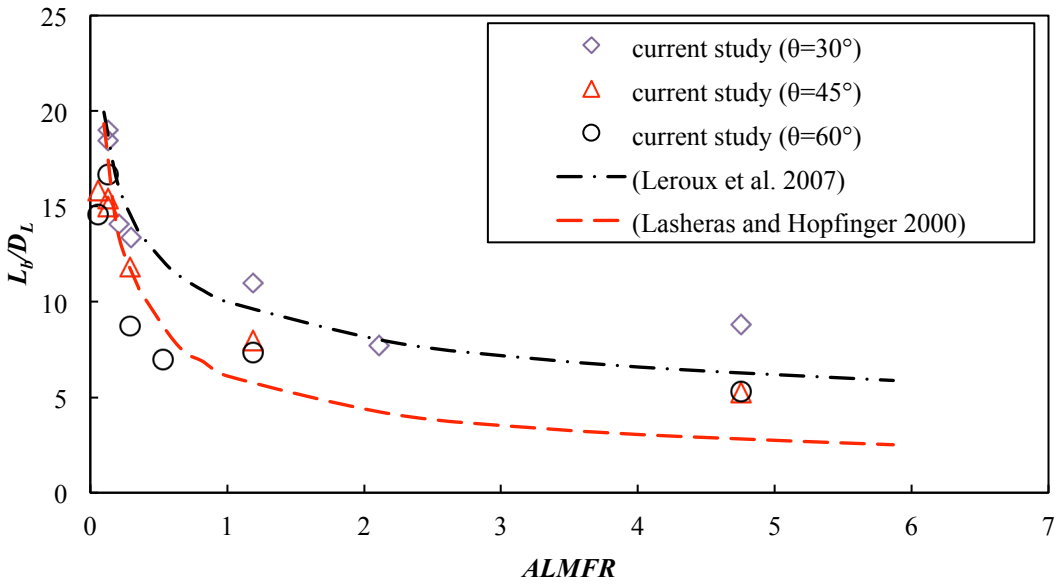

Fig. 9. Breakup length of the water jet as a function of *ALMFR* (air to liquid momentum flux ratio)

3.3 Spray angles

Spray angles are presented against *ALMR* (air to liquid momentum ratio), as defined in Eq. (3), and asserted as the appropriate parameter to describe air-liquid external impinging jets atomization process by Boden, et al. (1999) or for coaxial airblast atomizers by Engelbert, et al.

(1995). This parameter was selected, instead of ALMFR, in these publications in an attempt to scale the results for different nozzle dimensions. As shown in Fig. 10, both divergence and deflection angles (see Fig. 3) increase rapidly with increasing *ALMR* towards a constant value beyond *ALMR* = 4, which corresponds to the value of ALMFR =1. The saturation of the spray angles is due to the fact that the air jet penetrates the water jet and in general, the deflection angle is smaller than the divergence angle. For the divergence angle, the constant values are around 104°, 93° and 78° for jets impingement angles of 60°, 45° and 30° respectively. For the defection angle, values of around 35°, 50° and 72° are measured for jets impingement angles of 30°, 45° and 60°, respectively. Overall, a larger impinging angle leads to a larger spray angle due to the higher horizontal momentum of the water jet at a higher impingement angle, which leads to higher impact.

The results of Fig. 10 suggest that there is no reason to increase the air flow rate beyond a certain value for each liquid flow rate, because the spray angles will not change. Therefore, if the purpose is to control the spray angle using the air flow rate while we maintain the liquid flow rate constant, we can optimize the supplied energy input through the air stream.

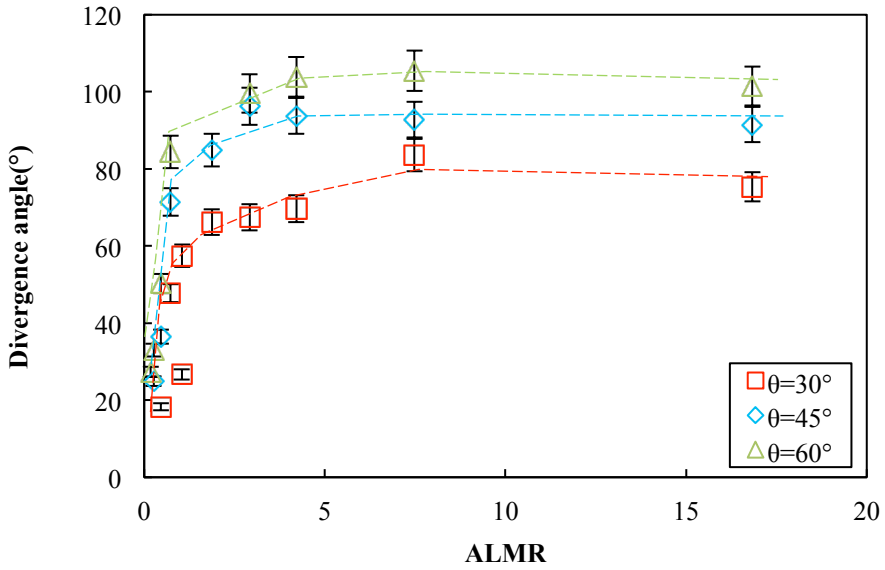

(a) Divergence angle α

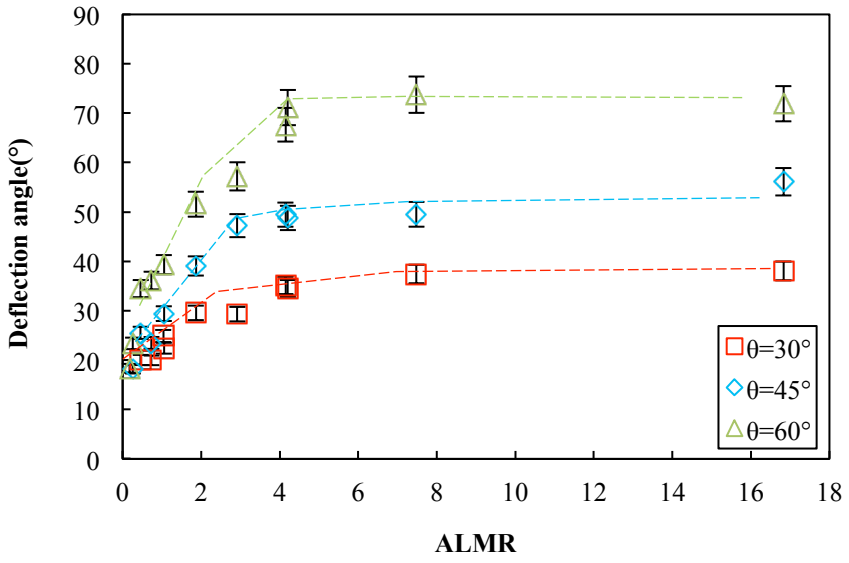

(b) Deflection angle β

Fig. 10. Spray angle distribution against *ALMR* (air to liquid momentum ratio)

3.4 Spatial distribution of droplet sizes and volume flux

Figure 11 displays D_{32} radial profiles measured for jets impingement angle θ = 45°, Q_L = 100 mL/min and $\dot{m}_g$ = 13.5 g/min on the cross sectional XY plane of the spray at distance z = 75 mm downstream of the impingement point from x = -30 mm, y = -40 mm to x = 30 mm, y = 40 mm. The axial distance of 75 mm was chosen so that the droplet sizes in the spray are stable and the spray distribution is representative, as will be explained later. Droplets located around the air jet axis are the smallest (around 50 µm) as a result of the strongest interaction between the air and liquid jet. We can distinguish two regions that extend on either side of the axis at x = 0 mm. The first one from x = 0 to x = 30 mm, i.e. on the side where the liquid jet is located, displays bell shaped profiles with the minimum droplet diameter in the central region and increasing towards the edges as y increases. As we move away from x = 0 mm, the droplet size also increases to reach an almost constant value at x = 30 mm of around 120 µm. On the other side, i.e. from x = -30 to x = 0 mm, the droplet diameter decreases to reach a minimum value of around 50 µm in the central region at x = -10 mm and increases again beyond this region to reach around 90 µm at x = -30 mm. The spatial distribution of the D_{32} of droplet sizes on this plane is presented as contours in Fig. 12 (b) to provide an easier representation of the spray than the radial profiles of Fig. 11. Fig. 12 (b) demonstrates that the spray is symmetrical around the Y-axis, but not around the X-axis.

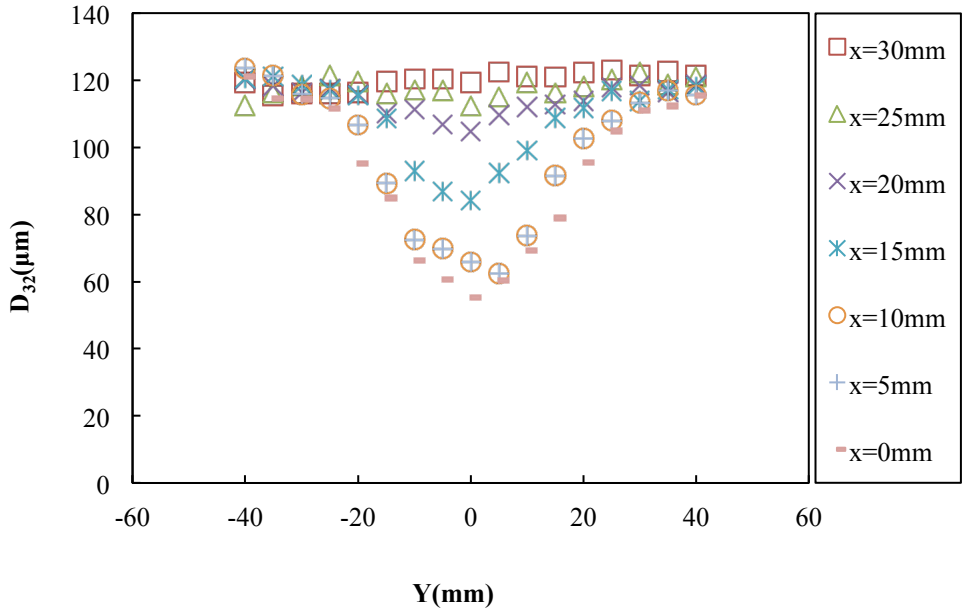

(a) x = 0~30 mm

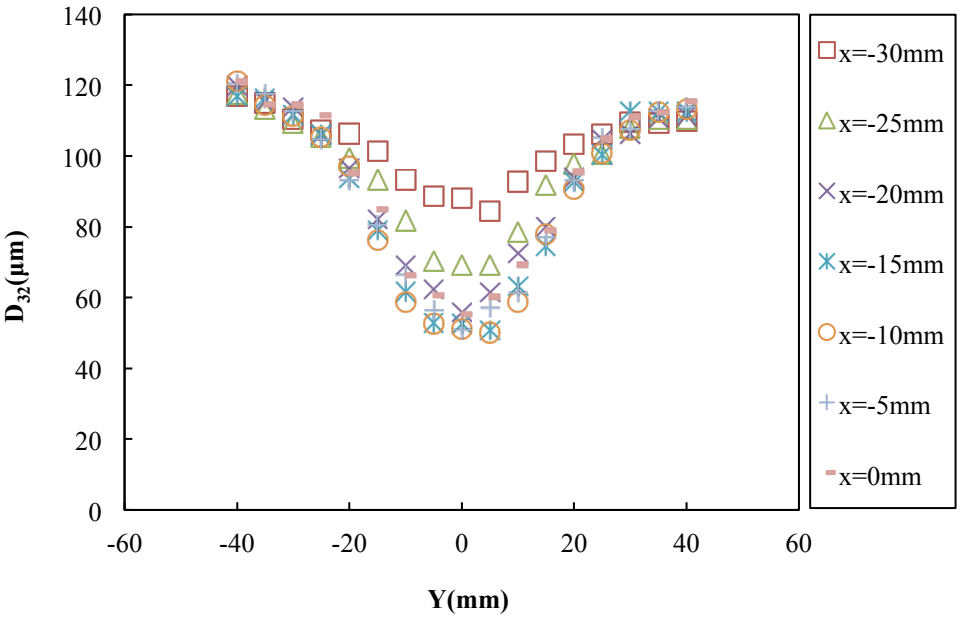

(b) x = -30~0 mm

Fig. 11. Spatial distribution of D_{32} on the plane of z = 75 mm in the spray of θ = 45°; Q_L = 100 mL/min; $\dot{m}_g$ = 13.5 g/min

Planar distributions of D_{32} and liquid volume flux at planes at different distances from the impingement point in the spray with θ = 45°; Q_L = 100 mL/min; $\dot{m}_g$ = 13.5 g/min are illustrated in Fig. 12 and Fig. 13, respectively. Results indicate that smaller droplets are located in the

region downstream of the impingement point and the droplet sizes increase towards the edge of the spray. The liquid volume flux is the largest in the central region of the cross section plane, corresponding to droplets of smaller sizes. The minimum Sauter mean diameter $(D_{32})_{min}$ decreases from 65 μm at z = 45 mm to 55 μm at z = 75 mm, suggesting possible secondary breakup of the droplets. The fact that $(D_{32})_{min}$ for z = 120 and 135 mm remains 55 μm indicates that the secondary droplet breakup is complete at z = 75 mm.

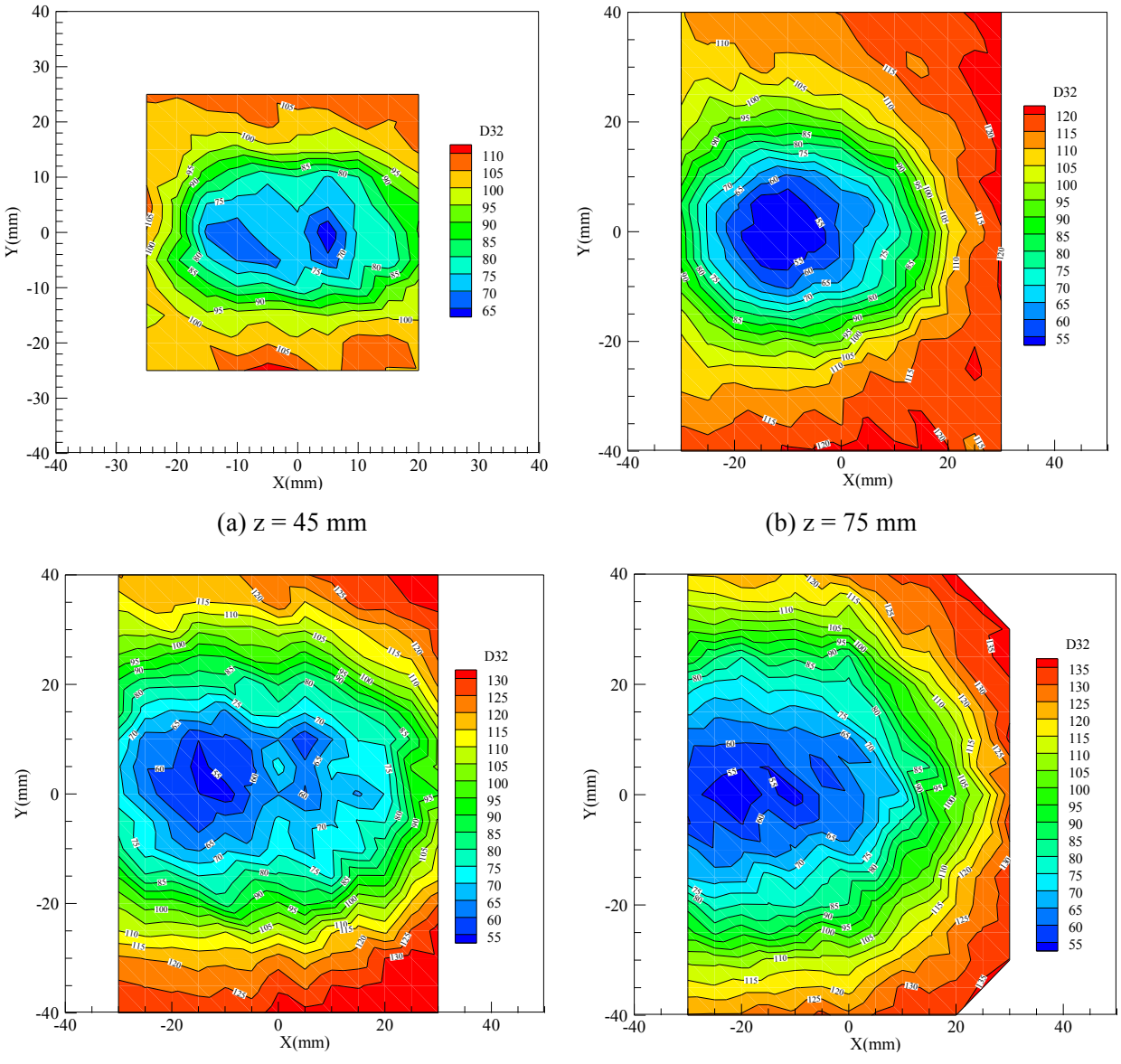

(a) z = 45 mm

(b) z = 75 mm

(c) z = 120 mm

(d) z = 135 mm

Fig. 12. Planar distribution of D_{32} (μm) at several axial locations in the spray with θ = 45°; Q_L = 100 mL/min; $\dot{m}_g$ = 13.5 g/min

It is clear from the contours of liquid volume flux with the unit of mL/cm^2·s in the axial direction that most of the droplets are located in the central region, which expands in the downstream direction. Droplets located in the central region of the spray have smaller sizes, thus the number of small droplets per unit time is much higher than large droplets at the outer region.

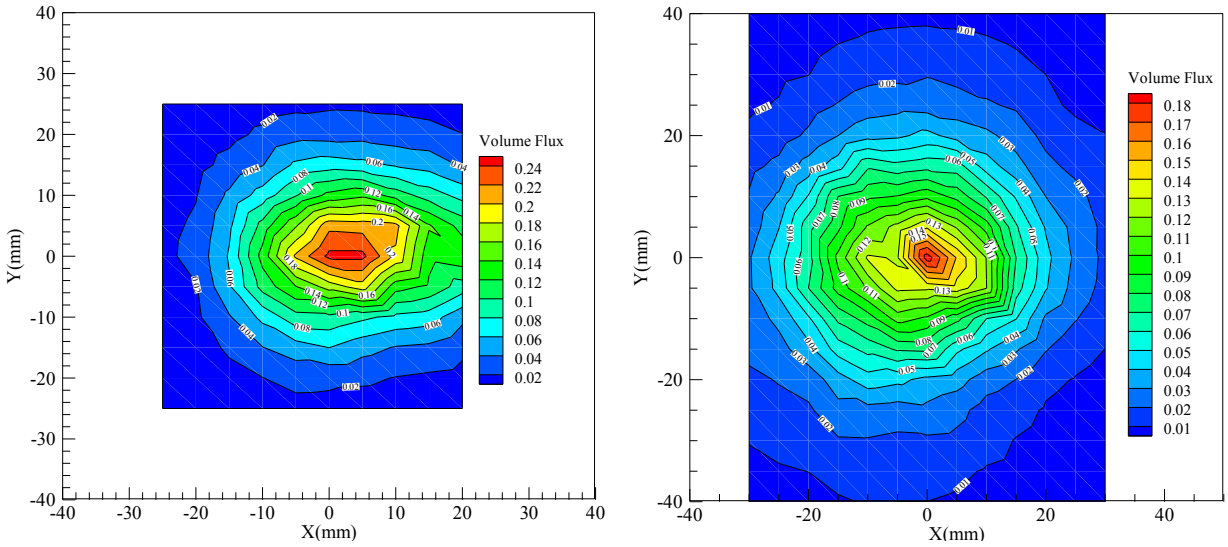

(a) z = 45 mm

(b) z = 75 mm

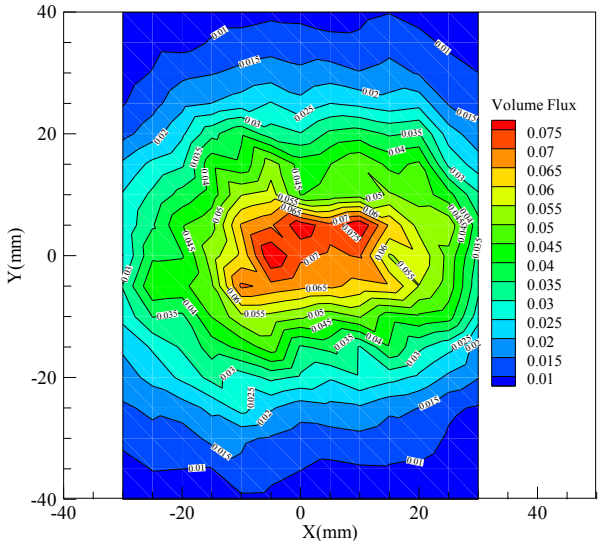

(c) z = 120 mm

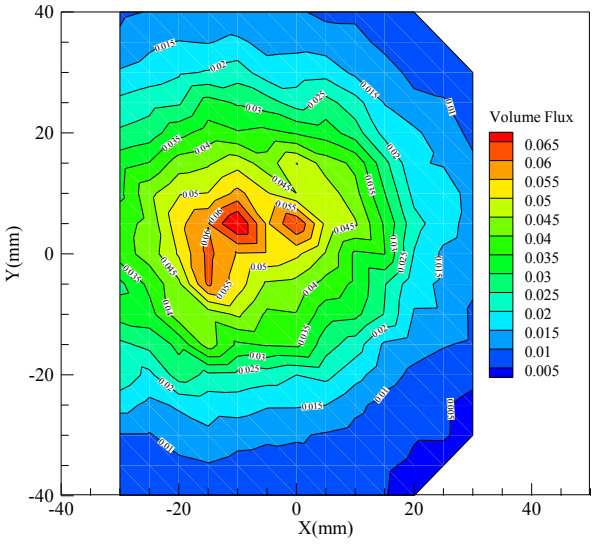

(d) z = 135 mm

Fig. 13. Planar distribution of liquid volume flux (mL/cm^2·s) in the axial direction at several axial locations in the spray with θ = 45°; Q_L = 100 mL/min and $\dot{m}_g$ = 13.5 g/min

The local values of D_{32} measured along the Z axis (at x = 0 mm) in the spray under conditions of θ = 45°; Q_L = 100 mL/min and $\dot{m}_g$ = 13.5 g/min are shown in Fig. 14 (a). D_{32} firstly decreases to about 55 µm at z = 75 mm, possibly due to the secondary breakup, and then increases beyond that point to around 60 µm at z = 175 mm. Two possible reasons are can be behind this subsequent increase. The first one, might probably be due to coalescence. However, because of the spray spreading characteristics along the Z-direction rendering the probability of droplet collision very low, this reason has to be ignored. The second one is due to dispersion; where different dispersion behaviors of different droplet sizes at the location of droplet formation, for example, larger droplets located in the edges of the inclined spray travel downwards and may be relocated in the central region of a lower cross section plane of the spray. Notwithstanding this explanation, the spatially-averaged SMD, calculated using Eq. (1), at several cross sectional planes of the spray for Q_L = 100 mL/min and $\dot{m}_g$ = 13.5 g/min is presented in Fig. 14 (b). It can be seen that the spatially-averaged SMD remains constant at around 82 µm for the same spray conditions. Comparison between the local D_{32} and spatially-averaged SMD indicates that the local value is not enough to represent the atomization quality of the spray. In addition, the possible behavior of the droplets between planes at z = 45 and 75 mm, i.e. droplet breakup or droplet collisions, does not occur, because the spatially-averaged values would also change. This result, therefore, consolidates the idea of choosing this spatially-averaged SMD as a criterion of evaluating the atomization quality for different operating conditions of the atomizer.

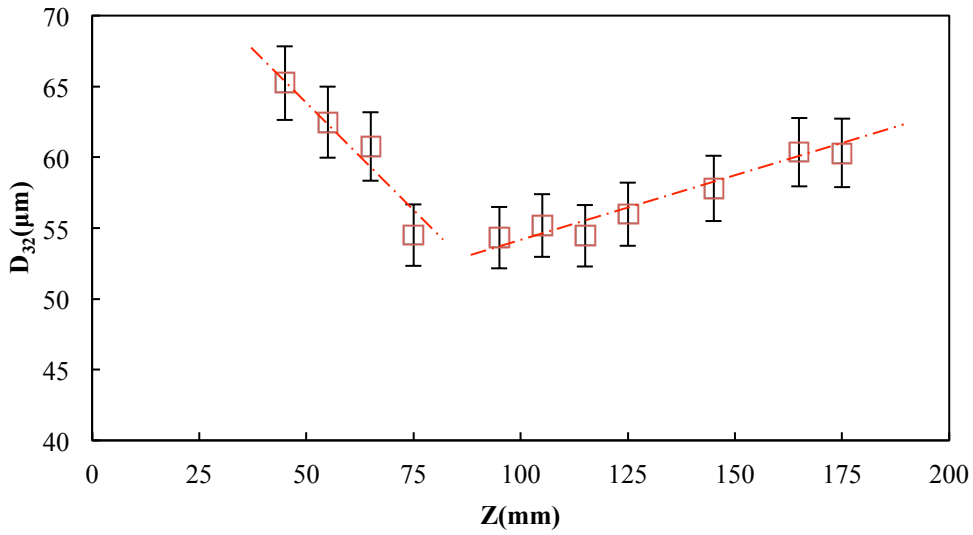

(a) Local D_{32} at x=0mm and different axial positions (line for visual aid only)

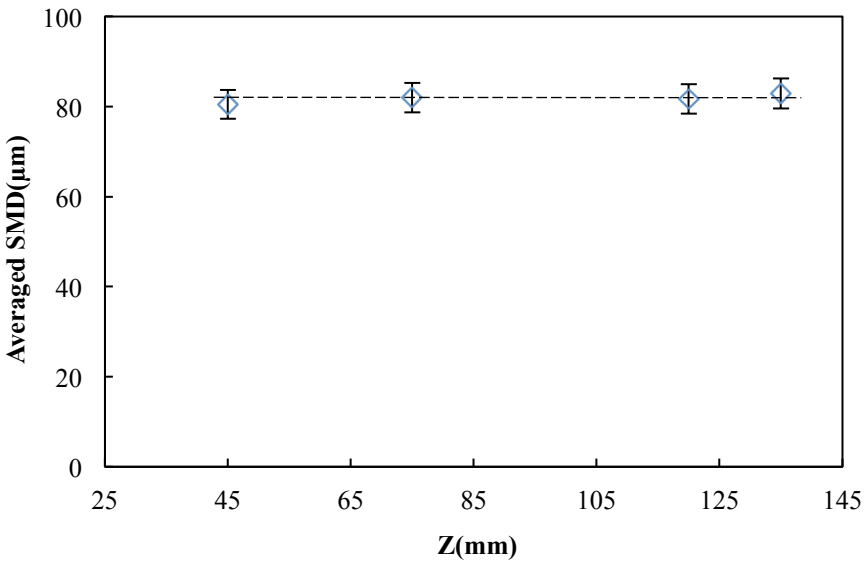

(b) Spatially-averaged SMD distribution

Fig. 14. Droplet size evolution as a function of the axial position in the spray for θ = 45°; Q_L = 100 mL/min; $\dot{m}_g$ = 13.5 g/min

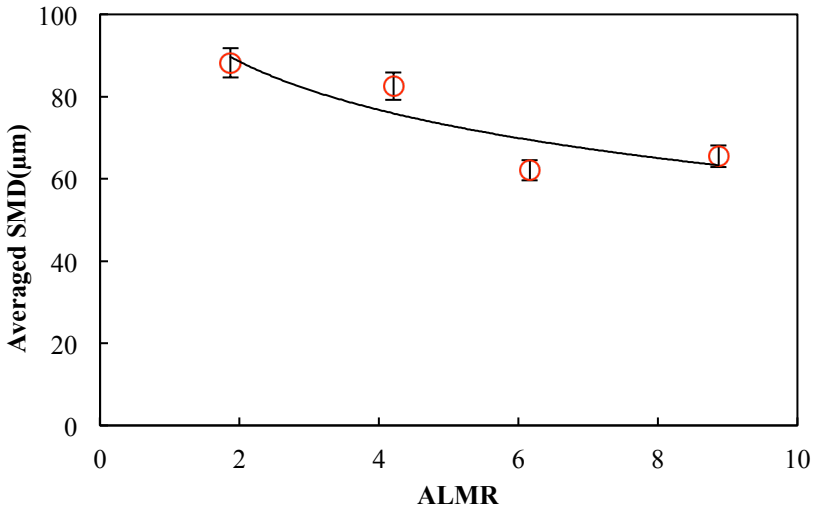

Fig. 15. Influence of ALMR on spatially-averaged SMD at θ = 45°

The spatially-averaged SMD, measured on the plane of z = 75mm, for sprays with different values of *ALMR* is illustrated in Fig. 15. It decreases gradually from 88 μm to 65 μm with the increase of *ALMR* over the range considered in the current study.

The effect of jets impingement angle on the spatially-averaged SMD is also investigated and results shown in Fig. 16 indicate that its effect is negligible, which means that the impingement

angle does not change the overall droplet size and, therefore, the atomization efficiency, but only affect the spray spatial distribution to some extent, as the contours of local droplet SMD and liquid volume flux distributions illustrate in Fig. 17 and Fig. 18. This behavior is in agreement with the findings of Boden, et al. (1999).

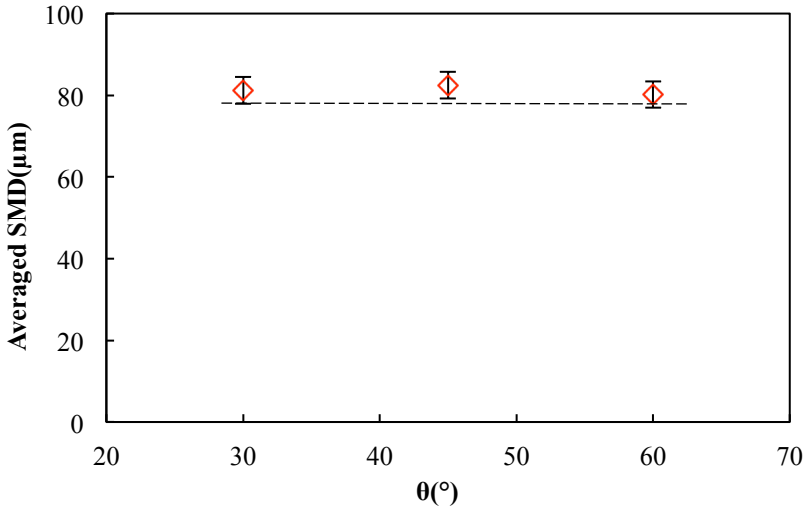

Fig. 16. Influence of jets impinging angle on spatially-averaged SMD at the plane with z = 75 mm in the spray with Q_L = 100 mL/min; $\dot{m}_g$ = 13.5 g/min

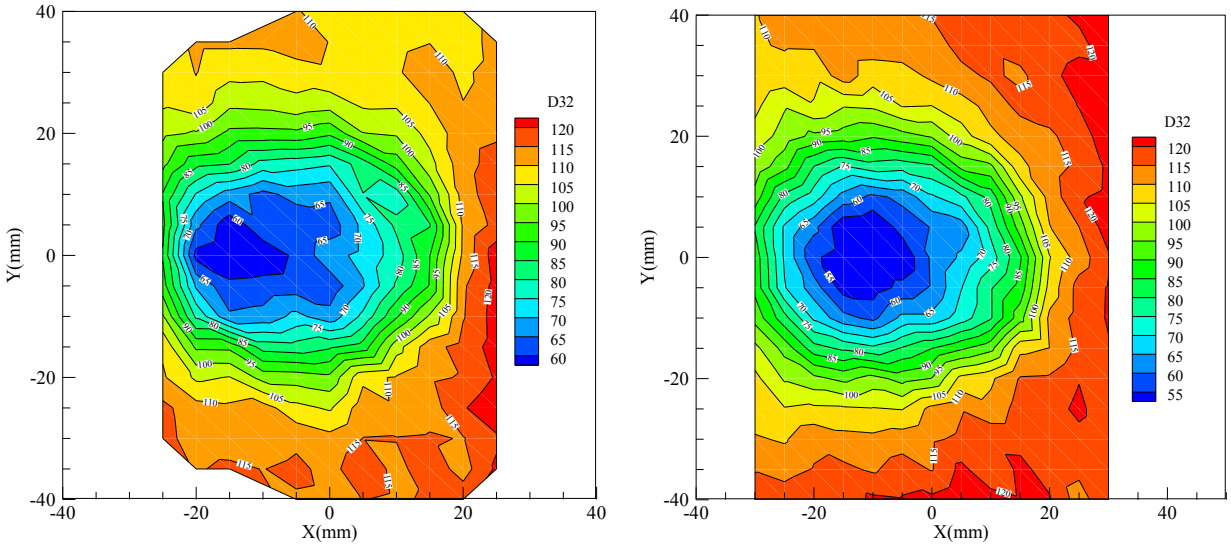

(a) θ = 30° (b) θ = 60°

Fig. 17. Influence of jets impinging angle on planar distribution of D_{32} (μm) at the plane z = 75 mm in the spray with Q_L = 100 mL/min; $\dot{m}_g$ = 13.5 g/min

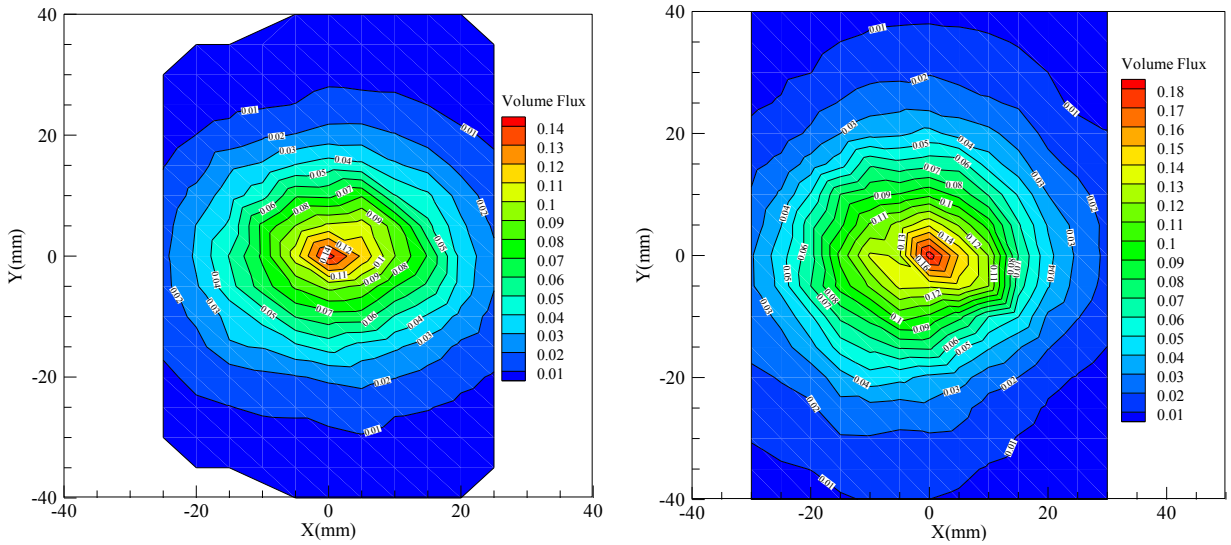

(a) θ = 30° (b) θ = 60°

Fig. 18. Influence of jets impinging angle on planar distribution of the liquid volume flux (mL/cm^2·s) in the axial direction at the plane z = 75 mm in the spray with Q_L =100 mL/min; $\dot{m}_g$ = 13.5 g/min

3.5 Droplet mean velocities and RMS of velocity fluctuations

The mean axial (along the Z direction) and radial (along the Y direction) velocity components of the droplets in the spray with θ = 45°, Q_L = 100 mL/min and $\dot{m}_g$ = 13.5 g/min are shown in Fig. 19. The axial velocity displays important spatial gradients, mainly within 15 mm around the air jet axis, while, outside of this region, gradients are relatively small. The mean velocity profiles are thus modulated by the air jet momentum. This explains why in this region the D_{32} of droplets is smallest, because of the strong momentum and shearing action provided by the air jet. The mean radial velocity has different directions on the two sides of the Y-axis, as expected, with relatively small values.

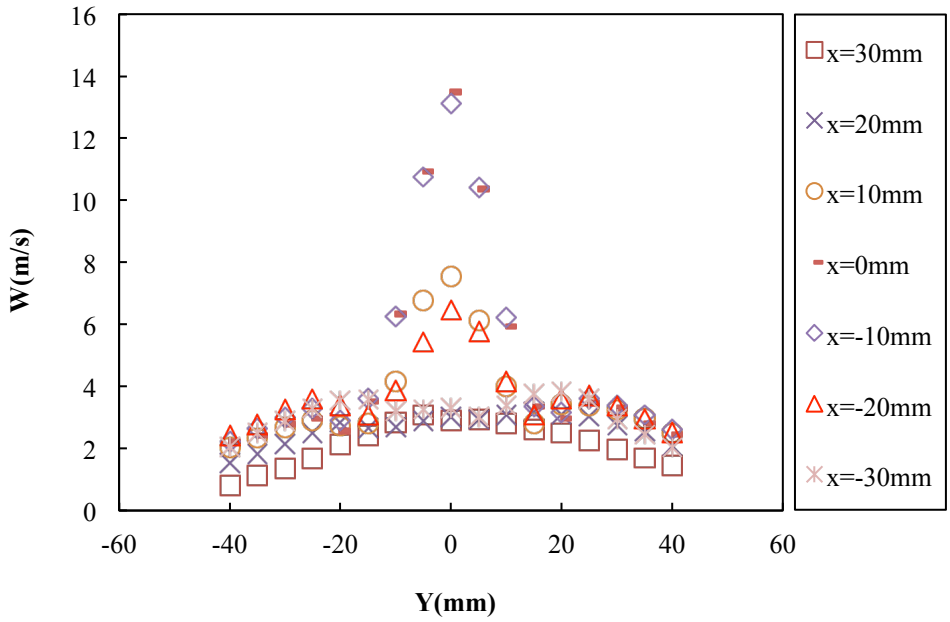

(a)

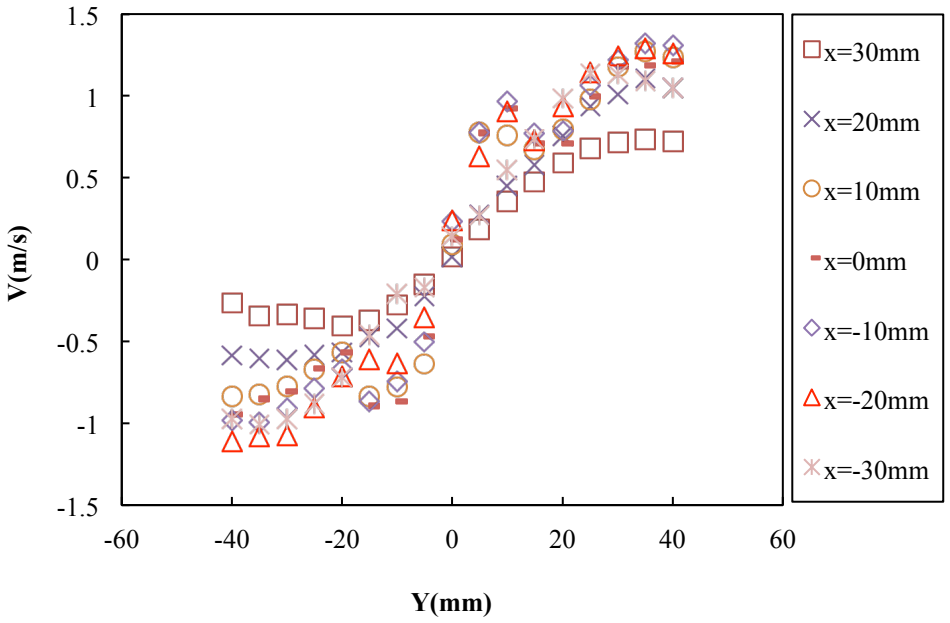

(b)

Fig. 19. Mean droplet velocity profiles at different locations on the plane of z = 75 mm in the spray with θ = 45°; Q_L = 100 mL/min; $\dot{m}_g$ = 13.5 g/min. (a) axial velocity; (b) radial velocity

The root mean square of the fluctuations of the axial and radial velocity components are shown in Fig. 20 and display different trends. The larger droplets located away from the spray central region have smaller RMS of velocity fluctuations, while the smaller droplets in the central part

display larger RMS values. This is probably due to the inability of the larger droplet sizes to follow the gas flow velocity fluctuations, while the smaller droplets have a better ability to do this. In addition, the droplet velocity fluctuations of the radial component are lower than those of the axial component by a factor between 2 and 3, which demonstrates the limited response of the droplet sizes to the gas flow velocity fluctuations. This leads to droplet trajectories in the spray, which move along straight lines in the spray over lengths longer than typical gas flow lengthscales. This droplet behaviour has been described as 'fan spreading effect' by Hardalupas, et al (1989) and leads to increase of the velocity fluctuations in the main flow direction, which is the axial direction in the current sprays.

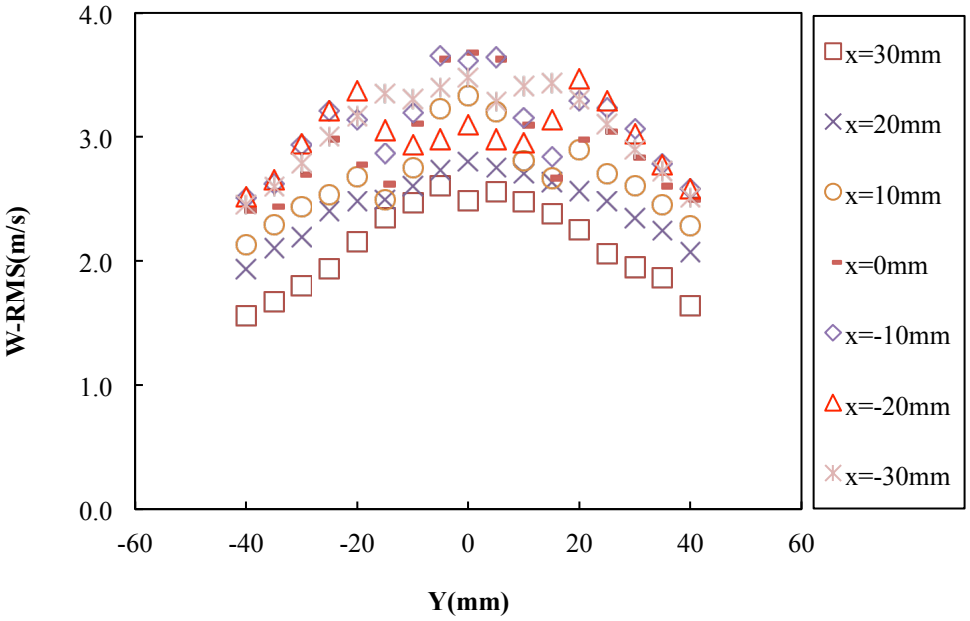

(a)

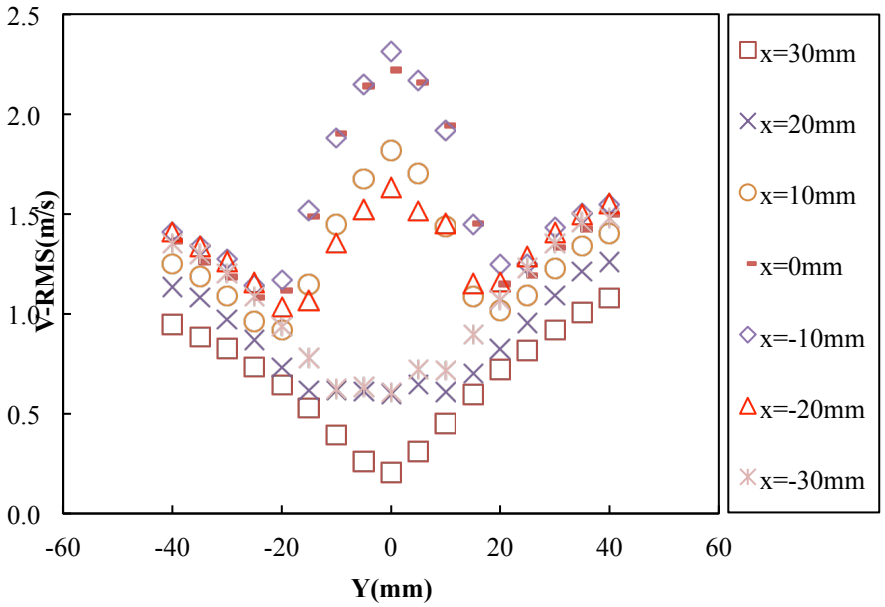

(b)

Fig. 20. Radial profiles of the RMS of droplet velocity fluctuations on the plane of Z=75mm in the spray with θ = 45°; Q_L = 100 mL/min; $\dot{m}_g$ = 13.5 g/min. (a) axial velocity; (b) radial velocity

Planar distributions of mean axial droplet velocity component, shown as contours, on planes at different axial positions from z = 45 mm to 135 mm in Fig. 21. It is clear that the maximum value of the droplet velocity decreases and the difference of mean velocity of droplets between the central and outer regions of the spray decreases with the increasing axial distance downstream of the jets impingement point.

The influence of jets impingement angle on the planar distribution of the mean axial velocity is illustrated in Fig. 22 by comparing the results for angles of 30° and 60°. The magnitude of the mean axial droplet velocity decreases by a small amount as the impinging angle increases from 30° to 60°. This is consistent with the negligible change of the spatially-averaged droplet diameter for different impingement angles, demonstrating the limited effect of the impingement angle on atomization and droplet motion. This suggests that the energy transfer from the air to the liquid remains the same when changing the impingement angles between 30° and 60°.

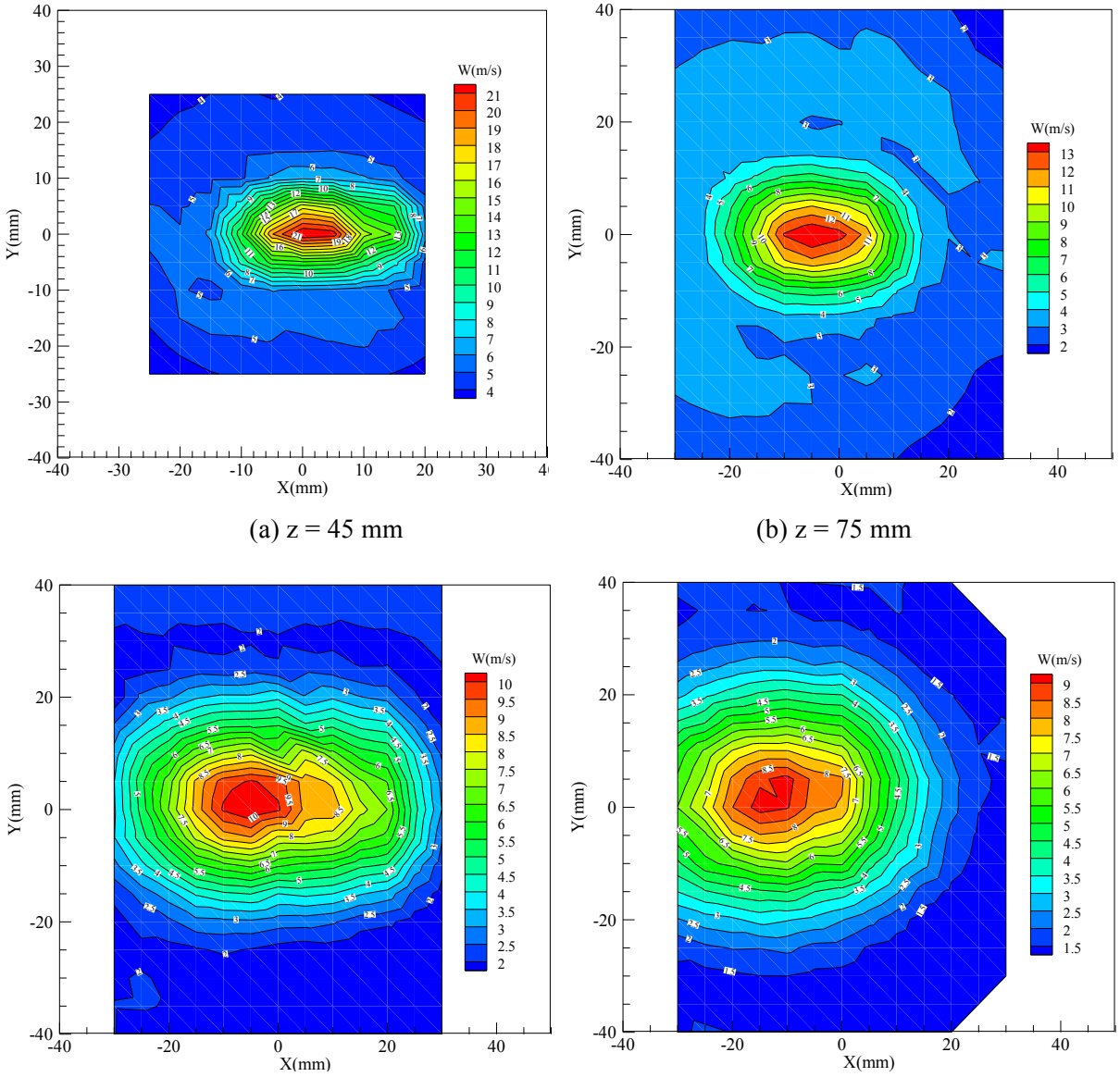

(a) z = 45 mm (b) z = 75 mm

(c) z = 120 mm (d) z = 135 mm

Fig. 21. Planar distribution of mean axial velocity W (m/s) at planes with different axial locations in the spray with θ = 45°; Q_L = 100 mL/min; $\dot{m}_g$ = 13.5 g/min

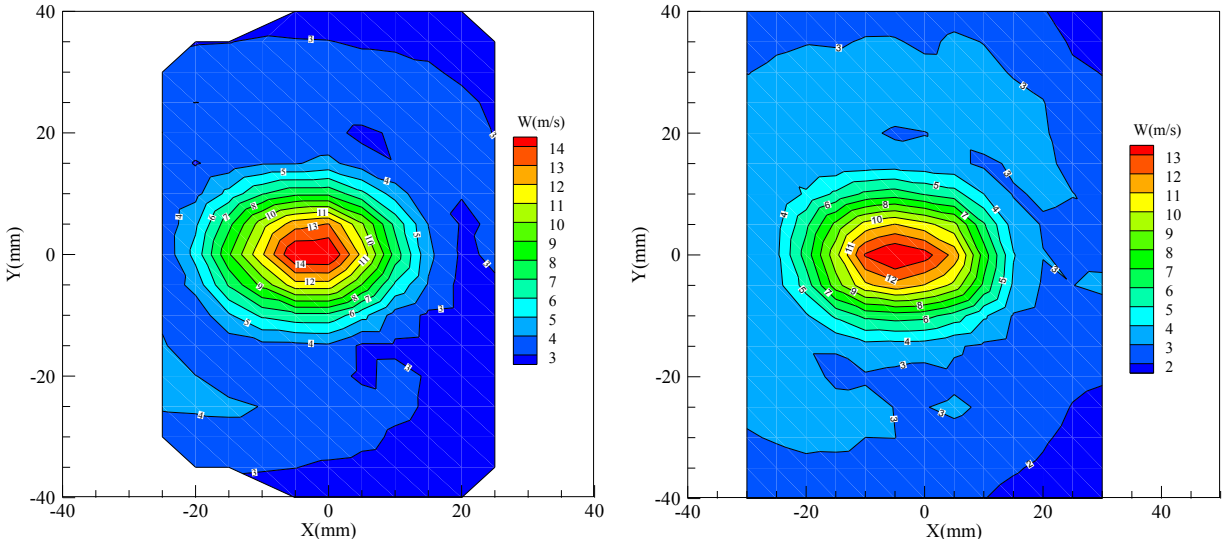

(a) θ = 30° (b) θ = 60°

Fig. 22. Influence of jets impinging angle on the planar distribution of mean axial droplet velocity W (m/s) on the plane of z = 75 mm in the spray with Q_L = 100 mL/min; $\dot{m}_g$ = 13.5 g/min

4. Conclusions

In this study, the characteristics of an air on water impinging jets atomizer is investigated. High speed photography and PDA are employed to conduct spray visualization and quantitative simultaneous measurements of droplet size and velocity and liquid volume flux in the resulting sprays.

From the spray visualization, some breakup regimes akin to those observed in co-axial airblast atomizers are identified. Liquid jet breakup length and spray angles are measured from near- and far-field images. It is found that L_b/d_l decreases from 20 mm to 7 mm as *ALMFR* increases by a factor of 6 for the case of impingement angle θ = 45°, and a larger impinging angle results in a shorter breakup length. The divergence angle reaches the constant values of 104°, 93° and 78° for impingement angles of 60°, 45° and 30°, respectively, and the defection angles remain as 35°, 50° and 72° for impingement angles 30°, 45° and 60° respectively, as the *ALMR* is larger than 4. Generally, the spray angles are larger for larger impinging angles, because of the beneficial effect produced by the horizontal component of the water jet momentum.

The mean size of water droplets on the cross-section plane of the spray at Z = 75 mm downstream of the impingement point was measured under conditions of Q_L = 100 mL/min, $\dot{m}_g$ = 13.50 g/min, and θ= 45°. Two regions extending on either side of the axis x = 0 due to the

deflection of the spray can be distinguished. From x = 0 to x = 30 mm, the planar distribution of local droplet D_{32} displays bell shaped profiles with $(D_{32})_{min}$ in the central region and increasing towards the edges as y increases. Along the X-axis from x = 0 to x = 30 mm, D_{32} also increases to reach an almost constant value around 125 μm. In the region from x = 0 to x = -30 mm, the droplet diameter decreases to reach a minimum value of around 50 μm in the central region at x = -10 mm and increases again beyond this region to reach about around 80 μm at x = -30 mm. The local value of D_{32} measured along the spray Z-axis at x = 0 mm decreases firstly to the minimum value at z = 75 mm and then increases again. However, the spatially-averaged values of SMD for the same spray conditions is about 82 μm for cross-section planes at different axial positions, which is also not affected to the change of the impinging angle. This finding demonstrates that the spray characteristics do not change due to secondary breakup or droplet collision leading to coalescence at the droplets move between different axial positions. However, with the increase of *ALMR*，the spatially-averaged SMD decreases by a factor of around 1.4 within the range considered in the current study.

The mean axial velocities of droplets are largest in the central region of the spray along the air jet axis and are thus modulated by the air jet velocities and decrease towards the edge of the spray at Q_L = 100 mL/min, $\dot{m}_g$ = 13.50 g/min and θ = 45°. The mean radial velocity has similar values on either side of the Y-axis, but with opposite directions. The magnitude of the radial velocity is however relatively small. The root mean square of the velocity fluctuations is larger in the central region of the spray, where the droplets are smallest with high velocities, while the opposite is true away from the central region.

Acknowledgements

The authors gratefully acknowledge the support from Khalifa University of Science and Technology, Petroleum Institute, Abu Dhabi, UAE in the form of a visiting graduate research assistant grant to Y. Xia.

References

Avulapati, M. M., & Ravikrishna, R. (2015). Experimental studies on air-assisted atomization of Jatropha pure plant oil. Atomization and Sprays, 25(7).

Avulapati, M. M., & Venkata, R. R. (2013). Experimental studies on air-assisted impinging jet atomization. International Journal of Multiphase Flow, 57, 88-101.

Boden J. C., Hardalupas Y., Krenteras P., Taylor A.M.K.P. P. (1999). Spray characteristics from free impinging air and liquid jets. Proc. 15th ILASS-Europe 99, Toulouse.

Chigier, N., & Farago, Z. (1992). Morphological classification of disintegration of round liquid jets in a coaxial air stream. Atomization and Sprays, 2(2).

Collins, T. J. (2007). ImageJ for microscopy. Biotechniques, 43(1 Suppl), 25-30.

Engelbert C., Hardalupas Y. & Whitelaw J.H. (1995) Break-up phenomena in coaxial airblast atomizers. Proc. Roy. Soc. Lond. A 451, 189-229.

Gañán-Calvo, A. M. (2005). Enhanced liquid atomization: From flow-focusing to flow-blurring. Applied physics letters, 86(21), 214101.

Gomez, J., Fleck, B. A., Olfert, J. S., & McMillan, J. (2011). Influence of two-phase feed bubble size on effervescent atomization in a horizontal nozzle assembly. Atomization and Sprays, 21(3).

Hardalupas Y., Taylor A.M.K.P. & Whitelaw J.H. (1989) Velocity and particle-flux characteristics of turbulent, particle-laden jets. Proc. R. Soc. Lond. A 426, 31 – 78.

Hopfinger, E. (1998). Liquid jet instability and atomization in a coaxial gas stream Advances in Turbulence VII (pp. 69-78): Springer.

Husted, B. P., Petersson, P., Lund, I., & Holmstedt, G. (2009). Comparison of PIV and PDA droplet velocity measurement techniques on two high-pressure water mist nozzles. Fire safety journal, 44(8), 1030-1045.

Inoue, C., Watanabe, T., Himeno, T., & Uzawa, S. (2013). Impinging Atomization Enhanced by Microjet Injection-effect, mechanism and optimization 49th AIAA/ASME/SAE/ASEE Joint PropulsionConference (pp. 3705).

Jadidi, M., Moghtadernejad, S., & Dolatabadi, A. (2016). Penetration and breakup of liquid jet in transverse free air jet with application in suspension-solution thermal sprays. Materials & Design, 110, 425-435.

Jedelsky, J., Jicha, M., Slama, J., & Otahal, J. (2009). Development of an effervescent atomizer for industrial burners. Energy & Fuels, 23(12), 6121-6130.

Jiang, L., Agrawal, A. K., & Taylor, R. P. (2014). Clean combustion of different liquid fuels using a novel injector. Experimental Thermal and Fluid Science, 57, 275-284.

Kourmatzis, A., & Masri, A. (2015). Air-assisted atomization of liquid jets in varying levels of turbulence. Journal of Fluid Mechanics, 764, 95-132.

Lai, W., Shakal, J., & Troolin, D. (2013). Accuracy, Resolution, and Repeatability of Powersight PDPA and LDV Systems. TSI Technical Note P(5001520), A4.

Lasheras, J. C., & Hopfinger, E. (2000). Liquid jet instability and atomization in a coaxial gas stream. Annual Review of Fluid Mechanics, 32(1), 275-308.

Lefebvre, A. (1985). Fuel effects on gas turbine combustion-ignition, stability and combustion efficiency. ASME J. Eng. Gas Turbines Power, 107(1), 24-37.

Lefebvre, A. (1988). Atomization and sprays (Vol. 1040): CRC press.

Leroux, B., Delabroy, O., & Lacas, F. (2007). Experimental study of coaxial atomizers scaling. Part I: dense core zone. Atomization and Sprays, 17(5).

Leroux, S., Dumouchel, C., & Ledoux, M. (1996). The stability curve of Newtonian liquid jets. Atomization and Sprays, 6(6).

Lubarsky, E., Zinn, B., Shcherbik, D., Bibik, O., & Gopala, Y. (2012). Fuel jet in cross flow-experimental study of spray characteristics. Advanced Fluid Dynamics. INTECH.

Niguse, Y., & Agrawal, A. (2016). Low-Emission, liquid fuel combustion system for conventional and alternative fuels developed by the scaling analysis. Journal of Engineering for Gas Turbines and Power, 138(4), 041502.

Prabhakaran, R., & Basavanahalli, R. (2013). Gas-on-Liquid Impinging Injectors: Some New Results 49th AIAA/ASME/SAE/ASEE Joint PropulsionConference (pp. 3706).

Rink, K., & Lefebvre, A. (1986). Influence of fuel drop size and combustor operating conditions on pollutant emissions: SAE Technical Paper.

Schneider, C. A., Rasband, W. S., & Eliceiri, K. W. (2012). NIH Image to ImageJ: 25 years of image analysis. Nature methods, 9(7), 671.

Simmons, B. M., & Agrawal, A. K. (2010). Spray characteristics of a flow-blurring atomizer. Atomization and Sprays, 20(9).

Sovani, S., Sojka, P., & Lefebvre, A. (2001). Effervescent atomization. Progress in Energy and Combustion Science, 27(4), 483-521.

Strasser, W., & Battaglia, F. (2017). The effects of pulsation and retraction on non-Newtonian flows in three-stream injector atomization systems. Chemical engineering journal, 309, 532-544.

Xia, Y., Khezzar, L., Alshehhi, M., & Hardalupas, Y. (2017). Droplet size and velocity characteristics of water-air impinging jet atomizer. International Journal of Multiphase Flow, 94, 31-43.